ELSEVIER

Contents lists available at ScienceDirect

Acta Astronautica

journal homepage: www.elsevier.com/locate/actaastro



Review article

Plume-surface interactions: A review of experimental work

Claudia Jimenez Cuesta ^{a,*}, Jack Davies ^a, Kevin Worrall ^a, Andrea Cammarano ^b, Hossein Zare-Behtash ^{b,c}

- ^a Space and Exploration Technology Group, James Watt School of Engineering, University of Glasgow, Glasgow, G12 8QQ, UK
- b Department of Aeronautics and Astronautics, School of Engineering, University of Southampton, Southampton, S017 1BJ, UK
- ^c Emirates Aviation University, Dubai, United Arab Emirates

ARTICLE INFO

Keywords: Plume-surface interactions Cratering dynamics Retro-propulsion Planetary surface erosion Regolith Future exploration missions

ABSTRACT

During the final metres of the powered descent of Apollo 11, astronauts Neil Armstrong and Buzz Aldrin lost sight of the lunar surface. As the retro-rockets fired towards the lunar dust - or regolith - to decelerate the spacecraft, soil erosion occurred and the blowing dust led to severe visual obstruction. After a successful landing, the presence of dust continued to impact the mission with adverse effects including respiratory problems and difficulty in performing tasks due to clogging of mechanisms, amongst others. As these effects were observed in subsequent missions, the "dust problem" was identified as one of the main challenges of extra-terrestrial surface exploration. In this work, the focus is placed on dust dispersal, which arises from the interaction between a rocket exhaust flow - or plume - and the planetary surface. Termed plume-surface interactions (PSI), this field of study encompasses the complex phenomena caused by the erosion and lofting of regolith particles. These particles, which are ejected at high-speeds, can lead to damage to the spacecraft hardware or a reduction in functionality. Moreover, plumes redirected back towards the landers can induce destabilising loads prior to touch-down, risking the safety of the landing. To achieve a sustained presence on the Moon, as planned by NASA's Artemis programme, it is essential that PSI are well understood and mitigating measures are put in place, particularly if spacecraft are to land in the vicinity of lunar habitats. Although experimental work began in the 1960s and mission PSI were first recorded in 1969, a fundamental understanding of this phenomena has not yet been achieved. In this paper, a compendium of experimental PSI is presented, identifying the main challenges associated with the design of tests, stating important lessons learnt and the shortcomings of available experimental data and findings. Lastly, recommendations for future experimental work are presented.

1. Introduction

When a spacecraft approaches its target extra-terrestrial body, it enters a very short but extremely challenging mission phase: entry, descent and landing (EDL). To ensure the success and safety of a mission, a safe soft landing is required, in which the spacecraft is fully decelerated before touch-down. During entry and descent, aerodynamic decelerators are used: rigid aeroshells, which transform the spacecraft's kinetic energy into thermal energy, and supersonic parachutes [1]. To complete the descent and landing, parachutes alone are not sufficient, as low density atmospheres limit their effectiveness. To overcome this, supersonic retro-propulsive rockets are fired in the opposite direction of travel, decelerating the vehicle to speeds of the order of a few metres per second. In atmosphereless bodies, retro-propulsion is the only method by which spacecraft can be decelerated [2]. When the plumes from these retro-rockets impinge on the planetary surface, they

give rise to a complex phenomena termed plume-surface interactions (PSI) - a multi-physics, multi-variable problem involving rarefaction of gas flow and gas-granular interactions. As exhaust gases reach the regolith bed, the surface is eroded and particles are ejected at very high speeds, which can obstruct visibility and damage spacecraft hardware. This was observed in the sandblasted returned samples of the Surveyor 3 [3], where pitting and cracking were present [4]. It was predicated that the damage to the spacecraft would have been orders of magnitudes greater, had it not been shielded by a crater and instead been exposed directly to the spray of ejecta caused by the landing of the Lunar Module [4] or by its earlier flyby [5]. It was also estimated that the redirection of plumes, or "fountain flow", during the Surveyor's landing was responsible for the camera sandblasting damage, and for part of the dust residue found in the samples returned to Earth [6].

E-mail address: claudia.jimenezcuesta@glasgow.ac.uk (C.J. Cuesta).

https://doi.org/10.1016/j.actaastro.2024.09.021

Received 5 June 2024; Received in revised form 21 August 2024; Accepted 7 September 2024 Available online 2 October 2024

0094-5765/© 2024 The Authors. Published by Elsevier Ltd on behalf of IAA. This is an open access article under the CC BY license (http://creativecommons.org/licenses/by/4.0/).

^{*} Corresponding author.

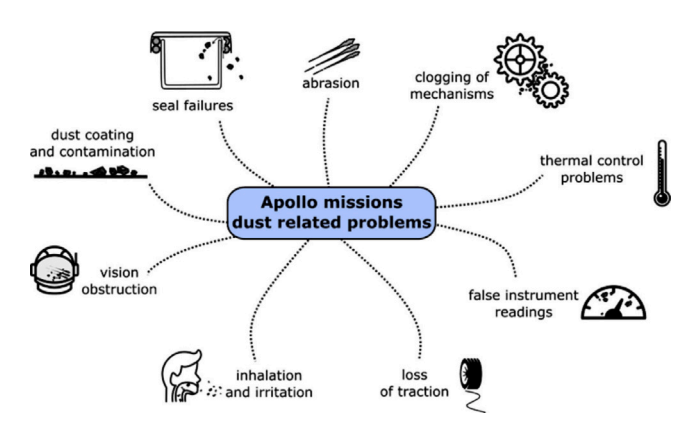


Fig. 1. Dust related problems chart from [8].

Many other dust-related problems were identified during the first Apollo missions, presented in Fig. 1. Dust coating on the astronauts suits and equipment lead to seal failures, clogging of mechanisms and thermal control issues [7]. Moreover, the presence of lofted dust introduced instrument errors, such as the false readings of the velocity trackers of Apollo 12. Lastly, astronauts experienced irritation of the respiratory tract due to the inhalation of dust, suggesting that further work by toxicologists and physicians was required to determine health risk related to dust exposure.

With planned missions expected to carry heavier payloads than ever before, such as the Starship's 150 tonne payload [9], and considering the estimation that PSI effects will scale up with spacecraft mass [6], there is growing concern about the risks posed to spacecraft robustness and crew safety by plume-surface interactions. It is expected that the negative effects of PSI will be present in all missions involving landing on celestial bodies, from large manned missions to planetary probes. This was evidenced by the landing footage of the Mars 2020 Perseverance Rover: during the skycrane manoeuvre, although the descent stage remained hovering at an altitude of 20 m, the lofted dust caused by the impingement of retro-rocket plumes obstructed the onboard cameras before touch-down, as seen in Fig. 2.

In this review paper, the problem of PSI is introduced, with a description of the main plume flow structures, the environmental conditions and planetary surface materials, the transitional regime in which plume flows rarefy, and the parameter space of PSI. A chronological literature review of experimental work is carried out, highlighting the main findings of each campaign, and collating the test matrices and measured variables in comparative tables. The five main erosion mechanisms identified are described, along with the scalable relationships developed to date and general observations from past tests. The challenges associated with experimental PSI are presented, and an evaluation of available diagnostic techniques and experimental procedures is carried out. Lastly, conclusions from the available work are drawn, identifying current gaps in the literature, and making suggestions for future work.

2. Physical conditions and variables of PSI

PSI is the umbrella term for all phenomena resulting from plume impingement on planetary surfaces. However, different regions surrounding the spacecraft are dominated by different physics, and hence should be considered in isolation to understand the problem as a whole. In this section, the PSI physical problem is divided into: (i) near-field flow physics (where the plume remains a continuum fluid), (ii) the environmental conditions and planetary surface materials (and their effect on plume behaviour and erosion), and (iii) the transitional regime (in which plume begins the process of rarefaction). Lastly, the

main variables involved are described, defining the parameter space of PSI.

2.1. Near-field flow physics

In the immediate vicinity of the retro-propulsive rockets of landers, the supersonic exiting flow has a Reynolds number of the order of 10^5 and a Knudsen number $\ll 1$, allowing the flow to be considered as a continuum [10,11]. Although for optimal efficiency the rockets' exit flow pressure P_e should coincide with the ambient pressure P_{atm} , this is rarely the case, and instead, flows are either over-expanded (if $P_e < P_{atm}$), under-expanded (if $P_e > P_{atm}$), or highly under-expanded (if $P_e > P_{atm}$). This mismatch in pressure gives rise to a series of compression and expansion waves that preserve the pressure across the resulting free boundary [12], also termed free jet or jet shock wave. Mixing with the surrounding air (from the environment) continues outside this boundary, in a region termed shear layer [13]. Lastly, the limit of the region where flow affects its environment is termed the jet boundary [14], indicated in Fig. 3.

2.1.1. Over and under-expanded flows

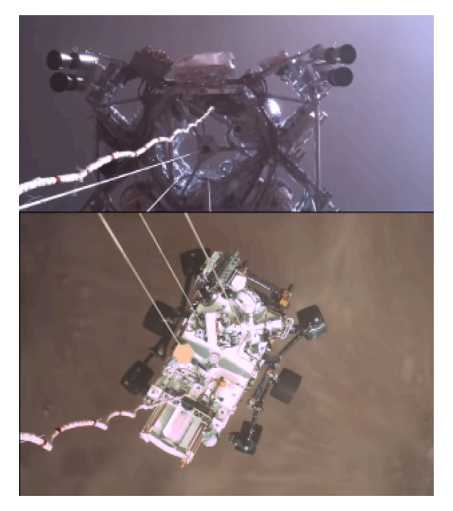
At the nozzle exit of over-expanded jets (Fig. 3(a)), oblique shock waves are formed, which increase the pressure of the flow. Due to the intersection of these shock waves, horizontal flow travels across two sets of pressure rises, which causes the flow pressure to exceed ambient pressure. To compensate, the oblique shock waves are reflected as Prandtl-Meyer expansion waves. However, these may cause the flow pressure to decrease below ambient pressure, requiring the expansion waves to be reflected as compression waves. This alternating pattern is repeated until a perfect match between flow pressure and ambient pressure is achieved. On the other hand, in under-expanded flows (Fig. 3(b)), the flow structure begins with expansion waves and follows the same pattern described, with alternating expansion and compression Prandtl-Meyer waves.

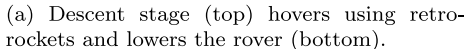
2.1.2. Highly under-expanded flows

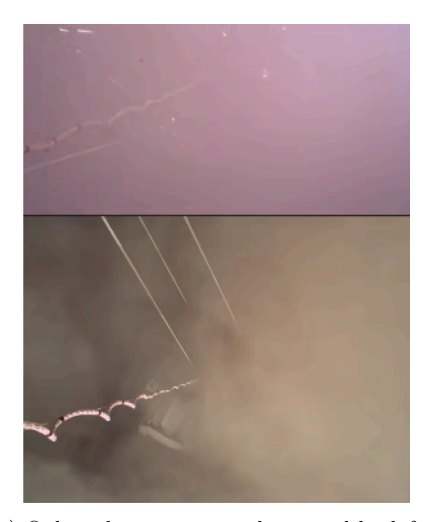
If the flow exit pressure is between 4 and 7 times that of the surrounding environment (4 < P_e/P_{atm} < 7), flows are considered to be highly under-expanded [13]. Under this condition, a slightly different structure is formed, termed barrel structure, shown in Fig. 4(a). In this figure, the compression and expansion waves are not indicated to avoid redundancy, but it is precisely the coalesced compression waves that cause its particular shape. Upon coalescence, these waves cannot undergo regular reflection, and instead, Mach reflection occurs. This leads to a Mach disc to appear perpendicularly to the flow direction and hence form a normal shock [14], as seen in the Schlieren image in Fig. 4(b). As with over and under-expanded jet flows, the structure is repeated until the ambient pressure is matched, which can be observed in the same Schlieren image, which displays a barrel structure with more than one cell. However, if $P_e/P_{atm} \gg 7$, the flow is considered to be very highly under-expanded and a unique barrel structure will be present [14], in which the Mach disc becomes a bow shock. In PSI occurring during lunar landings, the flow will always be highly under-expanded due to the surrounding vacuum, and will present the structures shown in Fig. 4(c). In this context, two additional structures will be present: a recirculation zone and a wall jet. The recirculation zone is found downstream of the bow shock and above the impingement zone, while the wall jet develops radially outside the impingement zone, due to the re-direction of the flow by the surface [16].

2.2. Environmental conditions and surface materials

The environmental conditions in celestial bodies are substantially different to those found on Earth's troposphere, and vary significantly across planets and other bodies (see Table 1). The Moon, with a surface gravity of $1.62~\text{m/s}^2$ and a very thin atmosphere [20], is considered to be in near-vacuum, while Mars, with a surface gravity of $3.71~\text{m/s}^2$







(b) Onboard cameras are obstructed by lofted surface particles.

Fig. 2. Footage from the Mars 2020 Perseverance Rover skycrane manoeuvre.

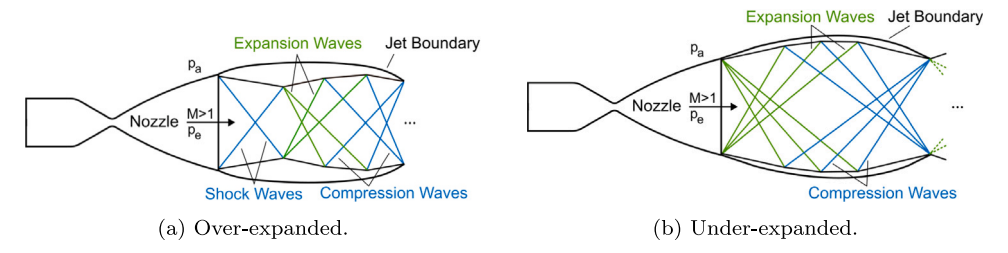


Fig. 3. Jet flow structures adapted from [14,15].

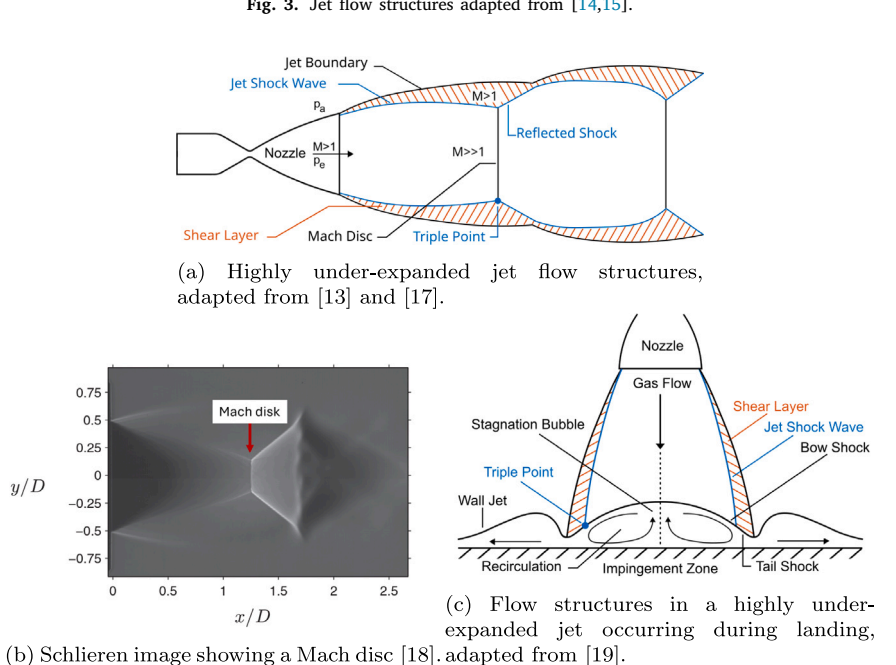


Fig. 4. Schematics and experimental image containing elements found in highly under-expanded jets [13,17-19].

and average ambient pressures between 400 and 870 Pa [21], has a more substantive atmosphere. As discussed in the previous section, depending on the surrounding environment, the plume structure will vary, which will have an effect on the erosion of the planetary surface. In Lunar landings, the retro-rocket plumes will be under-expanded as

the surrounding pressure tends to zero, while in Martian conditions, jet flows can be both over and under-expanded. In addition to erosion characteristics, ejecta speeds and trajectories will also be dependent on gravitational forces and drag forces, where the latter is a function of surrounding density.

Table 1
Approximate values of terrestrial, Lunar and Martian parameters [20,21].

	Gravity (m/s ²)	Pressure at surface (Pa)
Earth	9.81 (1g)	101 300
Moon	1.62 (0.17g)	~0
Mars	3.71 (0.38g)	636

Erosion mechanisms (presented in Section 4), will also vary with the properties of the planetary surface materials: particle size and particle size distribution will determine the cohesion of the soil, and hence its permeability, bearing capacity, and shear strength among others. Crater formation will depend on the friction of materials, with highly frictional materials resulting in steeper craters [22]. The unconsolidated upper layer of a planetary surface is termed regolith, and can vary in particle size distribution and mineral composition within the same planetary body. On the Moon, its two distinct regions contain different predominant materials: Lunar highland regolith, found in the heavily cratered and mountainous areas [23], is mainly composed of anorthosite and glass-rich basalt, while mare regolith, found in flatter regions, also contains a high proportion of pyroxene [24]. Moreover, Lunar regolith ranges from ultra fine particles (<1 µm), referred to as the Lunar dust, to larger unconsolidated rocks [25]. An understanding of the properties of regolith is essential in the context of particle entrainment arising from plume-surface interactions, but also in the design of astronaut protection equipment and spacecraft mechanisms. Much less information is available on Martian regolith, as the first two samples collected by the Perseverance rover are still to be returned to Earth, with current information being limited to in situ microscopic observations and wheel dynamics.

2.3. Transitional regime

Establishing the boundaries in which the plumes can be assumed to behave in a continuum manner will depend on the environmental conditions. On Mars, as the nozzle exit flow travels away from the thrusters, the surrounding atmosphere (and hence density) will collimate the plumes [26], making the flow parallel to the nozzle's centre line. This is due to the surface pressure resulting in an environmental Knudsen number $\ll 0.1$ and hence allowing the flow to be considered a continuum throughout its journey to the surface. On the other hand, the surrounding near-vacuum found on the Moon will cause the plumes to expand rapidly and transition into free-molecular flow regimes [27]. Identifying the transitional regime, including its location and characteristics, presents significant challenges in achieving high-fidelity numerical models of this phenomenon. While numerical modelling is crucial for PSI analysis, its intricacies justify a separate investigation, and therefore, it has been omitted from this review.

2.4. Parameter space

In addition to its multi-physics nature, PSI is a multi-variable problem with a prohibitively large parameter space. The variables can be divided into plume-related, environmental, and surface-related parameters. Firstly, plume-related variables consist of exit flow pressure, temperature, and Mach number, P_e , T_e , and M_e , respectively, mass flow rate \dot{m} , nozzle exit diameter d_e , impingement height h, and chemical composition of the exhaust flow. Secondly, environmental variables include atmospheric pressure and density, P_{atm} and ρ_{atm} , respectively, gravitational acceleration g, and surrounding gas composition. Lastly, surface variables include particle size d, particle size distribution, cohesion, internal structure, and chemical, mechanical and electrostatic properties. A combination of all these variables will result in a surface erosion characterised by its volume and rate, V and \dot{V} , and the ejection of particles with a given speed and ejection angle, v and α_e , respectively, and particle concentration.

3. Prior experimental research

A chronological review of past experimental campaigns is presented next. This is divided into early work, beginning in the 1960s and relating to Apollo and Viking missions; and recent efforts, beginning in the 2000s fuelled by a renewed interest in Lunar and Martian exploration.

3.1. Early work

The Apollo programme began in 1961 with the objective of developing the technologies that would allow mankind to land on the Moon and return safely to Earth. As part of the programme, a range of experiments were carried out during the 1960s and 1970s to test materials, components, and propulsion systems, which included the study of PSI. Leonard Roberts first investigated jet gas interactions with a granular medium in 1963 [28,29], defining semi-empirical viscous erosion and dust transport models based on shear stresses. Shortly after, experiments in vacuum conditions, carried out by Land, Clark and Scholl [30,31] at NASA's Langley Research Center (shown in Fig. 5) studied soil erosion and crater formation upon jet impingement at different heights.



Fig. 5. PSI apparatus in the Langley Research Center vacuum chamber in 1966 [31].

X-rays were used to measure erosion crater profiles, which showed that both descent speed and the cohesive nature of the surface had an effect on crater size. Moreover, a range of particles were used, which allowed the dependency between particle size and erosion to be identified. These experiments concluded that higher descent speeds minimised the size of craters and that cohesive particles eroded less than non-cohesive particles. Light attenuation was also measured to qualitatively estimate obstruction in visibility resulting from lofted particles. Work by Clark [32] also included the testing of model Lunar landers to predict heating rates and induced pressures from surface-reflected exhaust gases. Normal impingement pressure and surface heating were found to be inversely proportional to rocket altitude, reaching a maximum at a certain altitude and radial location, as shown in Fig. 6. This behaviour was expected to be caused by shock-structure disturbances within the nozzle [32,33].

Studies were also carried out in ambient conditions by Alexander et al. [34], in which pressurised cold and hot gases were fired from

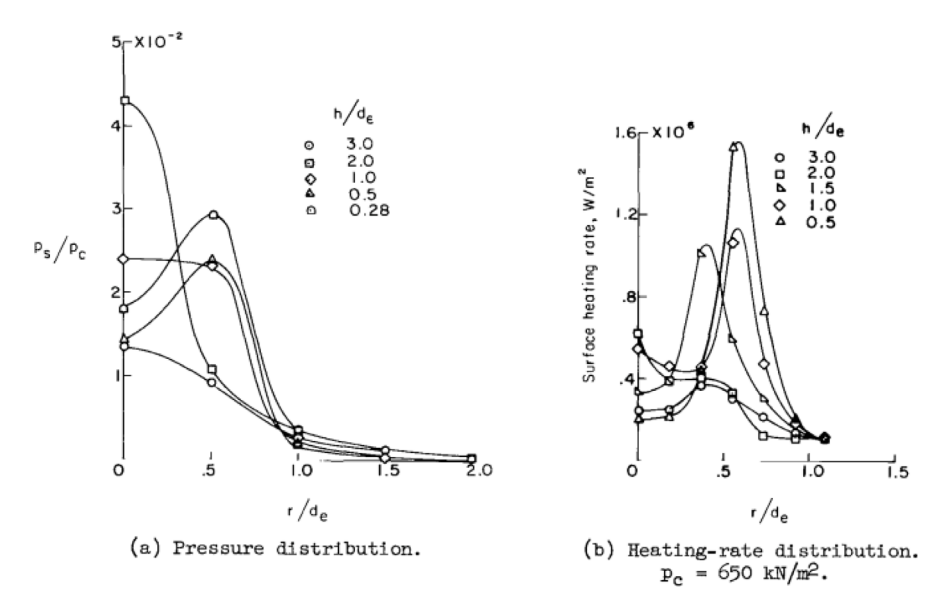


Fig. 6. Effect of rocket altitude on flat-surface pressure and heating [32].

different impingement heights, both stationary and with vertical velocities. This experimental campaign consisted of three separate tests: erosion characterisation from plume impingement in soil, pressure distribution measurements on flat and concave surfaces, and soil test analyses following hot firings. In these tests, a new erosion mechanism was discovered: explosive failure cratering, which occurred when the soil's material yield strength was exceeded by the pressure of the impingement jet, a process that could not be captured by Robert's viscous erosion model.

During the test firings of the Surveyor vernier engine in 1966 by Scott and Ko [35], it was observed that after engine shutdown, an annular crater formed in addition to the central crater previously seen in plume-surface interactions tests. It was hypothesised that this annular ring had not been caused by the entrainment of particles, but instead, the soil could have been removed by gas pressure in the pores of the soil. Consequently, through-depth pressure distributions were investigated, and a numerical analysis of axially symmetric flow with the boundary conditions of the Surveyor vernier engine was developed. Unlike Roberts' model, the granular surface was considered a porous permeable medium and Darcy's Law was applied to estimate transient flow transport into the surface. Their experiments unmasked another erosion mechanism previously unknown: diffused gas eruption. Therefore, it was concluded that the interaction of the plume with the granular medium could result in three separate erosion processes: transport of particles by the shear stress induced by gas flow (viscous erosion), rapid cratering by exceeding the soil's bearing capacity (termed bearing capacity failure, previously known as explosive failure cratering), and soil movement by upwards flow in an annular ring during firing or a central eruption after engine shut-off (diffused gas eruption).

In 1969, Mason et al. [36] performed vacuum experiments that estimated the Lunar Lander's crater depth and diameter, as well as establishing that the eroded volume was proportional to thrust and inversely proportional to the square root of the impingement height. Data from an in-situ experiment by Surveyor 5 [37] was also used to estimate erosion effects of the Lunar Module descent engine. However, a few years later, Scott [38] predicted a much higher erosion volume, based on the estimated number of particles required to cause the sand-blasting observed in Surveyor 3. In a similar manner, an inconsistency was identified by noting that the Apollo videos showed dust streak angle variations with time as the lander approached the surface [39], while the ejection angle was first assumed by Roberts to be independent of thrust level. It was evident, therefore, that neither erosion or ejecta

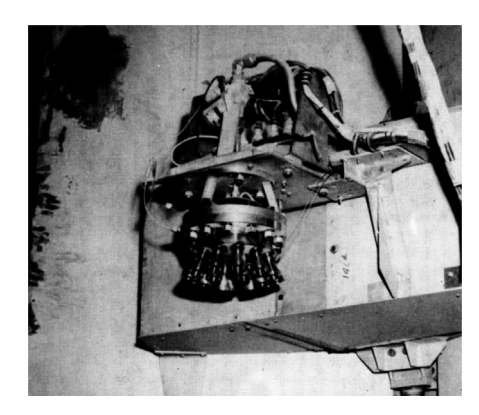


Fig. 7. Full-scale 18 nozzle configuration by Romine et al. in 1973 [41].

mechanisms had been properly understood prior to the landing of Apollo 11.

In preparation for the Viking missions, contemporary experiments focused on PSI arising in Martian landings. The effect of canting the three retro-propulsive rockets of the Viking lander was investigated by Clark et al. in 1970 [40], which concluded that this adjustment could achieve a reduction in ground erosion. Romine et al. [41] carried out an experimental and analytical investigation of rocket impingement in two phases: plume impingement pressure tests (Phase IA) and site alteration tests (Phase II). Their report suggested that the main bell nozzle of the lander be replaced by 18 small nozzles (shown in Fig. 7), such that the disturbance on the landing site was reduced to an acceptable risk level. Visual data taken during Viking landings confirmed the presence of erosion, both due to the obscuration of cameras attributed to dust cloud formation, as well as visible craters present after touchdown. Four Martian surface materials were observed: drift, blocky, crusty to cloddy, and rocks, and their respective predominant erosion processes were suggested [42,43].

3.2. Recent efforts

After the successful landings of the Apollo 17 and the Viking 1 & 2 missions in 1976, the programmes stopped as the focus shifted to Low-Earth Orbit missions, such as the International Space Station, commissioned in 1984. As a result, there is a gap in literature from the

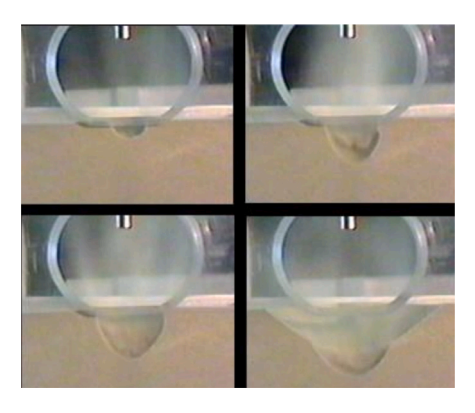


Fig. 8. Early PSI bisected experiments by Donahue et al. in 2005 [48] showing cratering development upon jet impingement.

1980s to the early 2000s, when PSI studies re-started in preparation for NASA's future missions to the Moon and Mars. In 2004, Philip Metzger emphasised the importance of studying gas-regolith interactions, drawing attention to landing consequences which were presented in studies dating from 1972 [44,45], such as the burial of the Viking footpad in Martian soil. He expressed the need to understand the physics involved in this complex phenomena, as cratering considerations would become drivers in spacecraft design and mission architecture [46].

This marked the beginning of a new era of erosion and cratering studies. Haehnel et al. [47] and Donahue et al. [48] carried out bisected jet half-plane cratering experiments (shown in Fig. 8) to develop growth rate scaling laws. It was found that although crater formation processes varied with thrust intensity, crater depth always increased logarithmically with time. A scaling law was defined to include physical constants, extending the equation which was first defined by Rajarantnam in 1982 [49]. Haehnel et al. [50] also extended Rajarantnam's equations to account for soil permeability and observed the dependence of crater shape on particle size.

Metzger continued the research and was the principal investigator during the following decade. From 2008 to 2010, small scale jet-induced erosion experiments were performed under atmospheric conditions using a range of gases, particle sizes, impingement heights, and exit velocities. In these experiments, behaviours were observed which contradicted Alexander's predictions [34], as a cutaway view of sand layers revealed upwards-pulled sand at the crater axis, as opposed to the expected downwards-bent layers [3]. To explain this, tests were repeated in a bisected manner for two speed regimes: the low velocity regime used high resolution videography and an automatic algorithm to extract crater shape and volume, whilst the high speed regime used high speed videography to qualitatively analyse particle movement [51]. It was observed that material was neither pushed down nor removed upwards as it was first thought, but instead, particles moved tangentially around the cavity, causing the coloured layers to deform upwardly. Hence, a new erosion mechanism was identified: diffusiondriven flow. It was also concluded that the rate of crater formation depended not only on soil ejection, but also on soil recirculation, which could be categorised into aerial, rolling, or deposit circulation. Next, tests with sieved quartz sand particles, and experiments in flying parabolic trajectories were carried out to adjust crater depth scaling laws in terms of particle size and reduced gravity, respectively [52]. Lastly, a material damage model was developed to predict the divots which could appear in the surfaces of hardware due to impacting particles, and an estimate for hardware damage as a function of landing site proximity was developed [53]. A summary of the aforementioned studies and their main findings has been compiled in [54].

Immer and Metzger [55] also performed three additional small experiments: the Handheld Observation of Scour Holes (HOOSH) and

Handheld Angle of Repose Measurements of Lunar Simulants (HARM-LuS), to investigate the effect of reduced gravity on crater formation and on the angle of failure of materials, respectively, and the Mars Architecture Team study (MATS), to explore the effects of compaction on the granular mechanics of crater development. HOOSH used a bisected setup and the post-processing of recorded videos to estimate crater depth, width and volume as a function of time. In a similar manner, HARMLuS used videography to record the angle of failure of different materials upon the rotation of cells containing previously levelled materials. MATS used high-speed videography to monitor craters upon supersonic rocket plume impingement on compacted and uncompacted JSC Mars-1A soil. A range of phenomena were observed in these studies, such as the increase in angle of failure with compaction and with decreasing gravitational acceleration. It was also concluded that the asymptotic crater depth was mainly dependent on firing duration, and on compaction to a lesser extent.

During the early 2000s, researchers of different fields contributed to the *Human Exploration of Mars Design Reference Architecture* document [56], a NASA report aimed at providing a vision and a common framework for future Mars exploration. This compendium included a chapter on landing plume effects, presenting experimental findings such as crater formation stages (deep cratering, broadening and collapse), and the risks associated with these, such as the tilting of spacecraft upon landing. Plume simulations were used to obtain blast zone predictions including impact velocity, momentum and energy as a function of particle size and distance. Lastly, a discussion on mitigation techniques such as shielding of landers and preparation of landing site were presented.

In 2014, Clark et al. [22] also studied sub-surface crater formation through a quasi-two-dimensional setup, which varied slightly from the three-dimensional half-space setup by Metzger, as the plumes in their experiments were not bisected. Lunar and Martian regolith simulants were used, and it was observed that horizontal symmetry breaking instabilities occurred in the Martian simulant test cases. It was suggested that in narrower craters (those occurring in highly frictional particle beds), debris exiting one side of the crater could be deposited in the opposite side, leading to uneven erosion. Then, a pitchfork bifurcation would occur, causing spontaneous breaks in the logarithmic crater growth with time. It was concluded that these instabilities would be of particular concern during spacecraft landings, as they could lead to a catastrophic loss of lander stability. In later work by Vessaire et al. [57], instabilities in crater formation were also attributed to oscillations in the plumes. Although their experiments used water jets, it was predicted that the coupling observed between the fluid and the surface particles would be present in many applications, including retro-rocket impingement.

In 2015, LaMarche et al. [58] investigated the effect of particle shape on crater formation in half-plane bevelled PSI experiments. It was found that non-spherical particles reduced crater width and volume but increased crater depth. Moreover, particle shape was observed to have a much more significant effect during the formation of the outer crater than during the initial inner crater formation. Their work also extended the asymptotic crater scaling relationship originally defined by Rajaratnam and Beltaos [59] to incorporate a shape factor.

In addition to these experiments, footage from the Apollo landings was studied to estimate mass erosion parameters. In 2008, Immer et al. [39] used photogrammetry to calculate dust ejection angle and lofted particle density from Lunar landing videos. Metzger et al. [54] calculated the optical density of the dust sheet and described in detail the phenomena observed during the landings, comparing these to field tests performed in the tephra of Mauna Kea [60]. The similarities found between the volcanic erosion tests and lunar landing videos allowed the available lunar data to be further interpreted. It was observed that only the finest dust particles (<10 μm) reflected light with enough brightness to be recorded, and considering the particle size distribution of lunar soil, this meant that about 90% of the mass of the soil was not

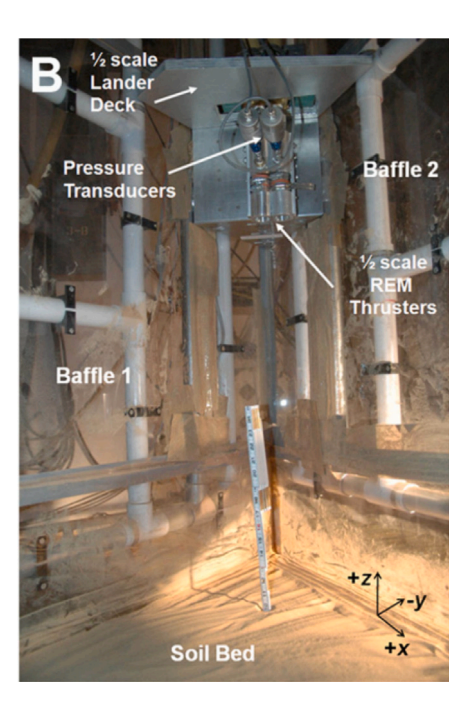


Fig. 9. Sub-scale Phoenix rocket motor setup at NASA Ames Research Centre's Planetary Aerolian Laboratory by Mehta et al. in 2011 [67].

visible in the recorded videos, even though the soil had been blowing in line-of-sight of the camera. Lastly, in 2015, Lane and Metzger [61] applied optical extinction measurements to estimate Apollo Lunar dust transport, following a methodology for rainfall intensity measurements used by the US Weather Service. An erosion rate scaling was defined to be proportional to the average shear stress to the power of 2.52, but this was later deemed incorrect due to the averaging methods used (personal communication by Metzger to the authors of this review). The relationship contradicted later results, and a new hypothesis was presented in more recent work [62,63].

As in the 1970s, PSI were also studied for Martian environmental conditions, a research effort lead by Manish Mehta during the early 2000s. In 2007, the first experiment focusing on supersonic pulsed rocket plume impingement took place [64], in which a half-scale model of the Phoenix thruster was fired into a plate with pressure sensors and into a soil bed (shown in Fig. 9). In their scaled model, the expansion ratio and the hypersonic similarity parameter were matched through a combination of thruster chamber pressure, pulse width, thrust, and motor frequency. Shadowgraph imaging was used for flow visualisation and, in combination with CFD simulations, flow structures were analysed. This resulted in the discovery of plate shock phenomenon, which would be further investigated during the following years (see [65] or the second chapter of Mehta's thesis, published in 2013 [17]). During his doctorate, he also discovered a fifth erosion mechanism: diffusive gas explosive erosion, arising from the use of pulsating jets and the induced shock waves. Lastly, he carried out experimental and numerical analyses that allowed the risks of the Phoenix and Mars Science Laboratory missions' landings to be assessed (presented in the third chapter of his thesis, [10,66,67]).

An insight into PSI in Martian landings was also achieved through the study of the Mars Science Laboratory descent footage by Vizcaino and Mehta in 2015 [68]. Through stereoscopic depth mapping, surface topography and features of the landing site were recreated. The four scour marks left on the surface by the lander's plumes were characterised in terms of crater geometry, eroded volume, and erosion rates, which were found to be in agreement with Mehta's prior ground tests.

In 2016, Metzger re-visited his work on atmospheric erosion scaling laws and performed experiments under Lunar environmental conditions [69]. In an attempt to incorporate the effect of rarefaction on

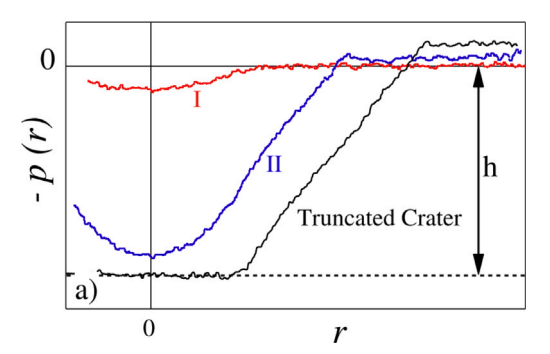


Fig. 10. Crater shape p(r) as a function of radial distance measured by Badr et al. [70].

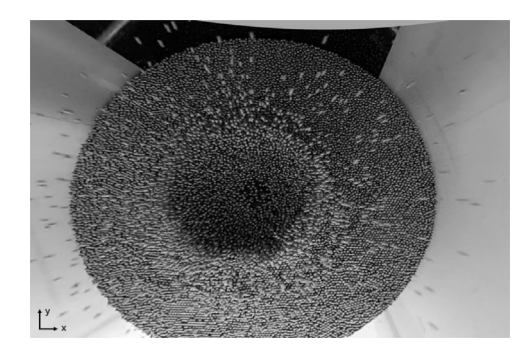


Fig. 11. Top-down view of a 50 ms pulse steel bead experiment in microgravity by Chambers et al. in 2020 [26].



Fig. 12. Side view of a 100 ms pulse steel bead experiment in microgravity by Chambers et al. in 2020 [26].

erosion, bisected tests at a range of Knudsen numbers were performed, from which it was concluded that the previously found scaling laws for continuum flow could not be used for rarefied flow and hence further tests were required to establish complete scaling relationships for Knudsen number variations. That same year, Badr et al. [70] studied the erosion resulting from a turbulent jet in atmospheric conditions as a function of Froude number. Using a profilometer, the crater shapes were measured and classified into two categories: parabolic (type I), and inner parabolic and outer conical (type II), shown in Fig. 10.

From 2016 to 2020, Chambers [26] investigated plume-surface interactions under vacuum microgravity, both computationally and experimentally. Firstly, gas diffusion in a regolith medium was modelled according to Darcy's Law in order to explore its role on regolith instability (see [71] or the second chapter in [26]). Secondly, a Gas Regolith Interaction Testbed (GRIT) was designed, consisting of a small vacuum chamber, a source of pressurised air, and a camera pair. The apparatus was released from a drop tower, allowing microgravity to be achieved and hence unmasking phenomena not present under 1g. Four different materials were tested (steel, glass, sand and CI Orgueil simulant), which proved that grain size, and hence permeability, had a

major effect on the predominant erosion process: larger grain sizes resulted in primarily diffusion-driven flow, whilst smaller grains induced mainly viscous shear erosion. Rough estimations of crater dimension and eroded mass were calculated using the camera's side and top-down views (shown in Figs. 11 and 12), and ejecta velocities were estimated using automated and manual particle tracking (see chapters 3 and 4 in [26]). His doctoral work concluded that increasing jetting time increased ejecta volume and reducing impingement height increased ejecta angle and eroded mass. Lastly, two new insights into erosion processes were uncovered: off-centre lofting and on-centre re-eruption, the latter being considered a single pulse case of diffusive gas explosive eruption.

Guleria et al. [72] performed half-plane subsonic atmospheric experiments with mono and poly-disperse glass beads to evaluate their impact on crater formation. They extended the classification first defined by Badr et al. into five crater shapes: saucer, parabolic, U-shape, parabolic with an intermediate region, and conical slants with a curved bottom. Each of these categories were observed in the experiments involving a mono-disperse particle bed, whilst for poly-disperse particles, only the first three shapes were present. They also observed a dependency between crater size and mass flow rate, and a linear increase of steady-state crater depth with mass flow rate.

In 2021, Masten Space Systems and the University of Central Florida investigated plume cratering effects through microgravity experiments, as first developed by Chambers, and ground tests [73]. Firing of hot plumes in terrestrial conditions allowed crater depth and diameter equations to be empirically defined, which were dependent on mass flow, impingement height and chamber pressure. Processes such as impact splash, slumping, or upward wave flow were also qualitatively discussed. Moreover, during the flight tests of Astrobotic's Xodiac rocket, the size and speeds of ejected particles were measured using the Ejecta Sheet Tracking, Opacity, and Regolith Maturity (STORM) instrument. Its configuration consisted of lasers and cameras which extracted cratering information from the transmitted and back-scattered light from the ejecta [74]. The same year, Metzger and Mantovani [75] estimated the damage that a spacecraft in the Lunar Orbital Gateway and Low Lunar Orbit would experience if impacted by regolith particles lofted by a lunar lander. In their damage model, they used erosion rate data from Rajaratnam and Mazurek [76] and work by the previous authors on erosion models and ejecta trajectories estimation [52,61]. It was concluded that further work was required to accurately predict damage potential, due to the gaps in knowledge in the predominant erosion physics.

Microgravity experiments were also performed by Baba et al. [77] at JAXA. A small scale-vacuum chamber was released from a drop tower, and the scattered sand grains upon the impingement of compressed air were visually studied. Although quantitative measurements were not recorded, the sand visualisation was used to validate simulation work.

NASA's most recent work, the Physics Focused Ground Test (PFGT) campaign, has been carried out under the PSI Project of the Game Changing Development Programme. Consisting of subscale, inert gas, bisected experiments, the campaign aims to study cratering and ejecta physics under Lunar and Martian conditions (Test 1), and impingement pressures and flow visualisation under Lunar conditions (Test 2) [78]. Qualitative results on crater profile growth were published in 2022 [79, 801, where a discussion on the effect of ambient pressure, mass flow rate and soil internal friction on crater shape was presented. Shown in Fig. 13, the observation of crater evolution with varying parameters allowed conclusions to be drawn, such as that higher mass flow rate resulted in craters with larger angles of repose. It was also observed that at low pressures, craters were wider and shallower, as opposed to the deep craters arising from the collimation of jets in higher ambient pressures. Later work by Gorman et al. [81] included quantitative analyses on erosion rates and scaling laws. A power-balance framework was used to quantify the time evolution of plume-induced cratering, and to define early-stage and late-stage erosion scaling laws.

Also within NASA's PSI project, Rodrigues et al. [82–84] investigated the flow structures of under-expanded and over-expanded supersonic jets in vacuum using planar laser-induced fluorescence (PLIF), while monitoring surface pressures. Significant differences in shock structures were observed in test cases of varying impingement altitudes, resulting in unexpected pressure distribution behaviours.

Thus far, most of the experimental work on PSI has focused on understanding and quantifying crater growth, and, in order to do so, bisected studies have been carried out, in which an external non-physical boundary has been introduced. To the best of the authors' knowledge, there are currently three research institutes developing non-intrusive PSI diagnostic techniques: Auburn University and the University of Illinois in the US, and the University of Glasgow in the UK.

At Auburn University, Stubbs et al. [85] developed a stereo photogrammetry system to obtain time-resolved 3D reconstructions of crater evolution resulting from plume impingement under atmospheric conditions. Their results showed that crater depth and radius exhibited a logarithmic growth with time, and an increase with reducing impingement height; both findings were in agreement with previous experimental work [48]. Their studies also concluded that the angle of repose, which is the steepest angle that granular materials hold before slumping, and crater volume both increased with increasing impingement height [86]. Based on the observed time-evolution of crater depth and erosion rates, it was suggested that at greater impingement heights, viscous erosion dominated, whilst at lower impingement heights, bearing capacity failure could be the main erosion mechanism present. Experiments were repeated in sub-atmospheric pressure conditions [87], measuring the depth, radius, and volume of the forming craters, as well as carrying out a qualitative comparison between atmospheric and sub-atmospheric crater formation. In 2024, Silwal et al. [88] published the continuation of this work, in which particle tracking velocimetry was added to their configuration, shown in Fig. 14. Through the tracking of ejecta, the measured trajectories were introduced into a ballistic model and used to estimate ejection velocity and angle through time regression. Moreover, the crater wall angle was calculated based on the stereo reconstruction performed, and it was found to vary with ejection angle. It was concluded that greater ejection velocities and lower ejection angles occurred for sub-atmospheric cases, compared to the ambient conditions test cases.

Stereo-photogrammetry was also applied by Crane et al. under reduced gravity drop tower experiments [89]. It was observed that low impingement pressures which did not result in surface erosion at 1g were substantial enough to eject particles at 0g. Additionally, it was found that a reduction in gravity increased crater volume and resulted in steeper craters.

At the University of Illinois, Rasmont et al. [90] designed and tested a dust cloud particle concentration system based on millimetre-wave interferometry. By measuring the phase shift between signals propagated in a particle-mixture and in a homogeneous medium, the volume fraction of ejecta was inferred. In their experiments, Lunar and Martian environmental PSI were tested, and the system was extended to include up to 7 reflectors (shown in Fig. 15(a)), allowing for a tomographic reconstruction to be achieved [91,92]. Moreover, ejecta phenomenology was observed using high-speed imaging, and the characteristics of the resulting craters were estimated by analysing still frames taken after the cratering events (shown in Fig. 15(b)).

The University of Glasgow hosts the European Space Agency's PSI facility, a dirty vacuum chamber with a 12 m³ volume test section, where experiments simulating landings in airless bodies and Mars are carried out. The desired ambient pressures can be maintained for extended periods, depending on the mass flow rate of the plume, achieved by using the 60 m³ buffer tank [93]. Current PSI research involves both the development of diagnostic techniques in atmospheric conditions and testing in sub-atmospheric conditions, with separate research groups focusing on the Lunar and Martian case. Cuesta et al. [94,95]

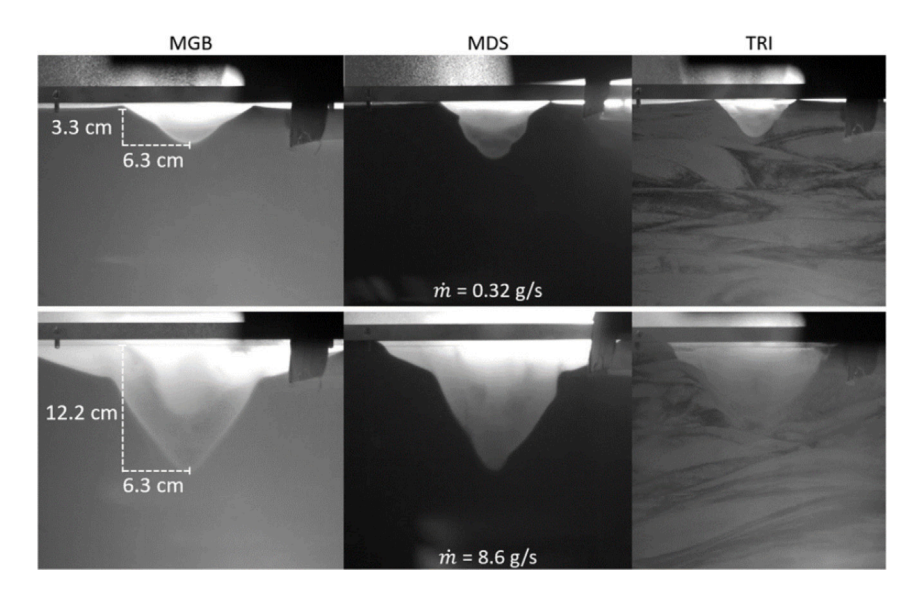


Fig. 13. Crater profiles variation with mass flow rate for mono-disperse glass bleads (MGB), mono-disperse sand (MDS) and tri-disperse particles (TRI) from [80].

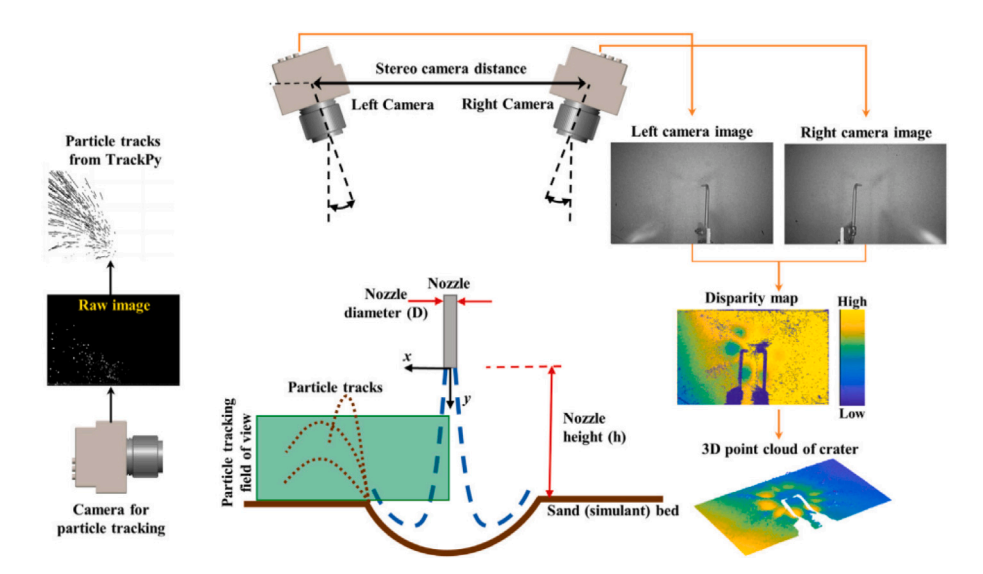
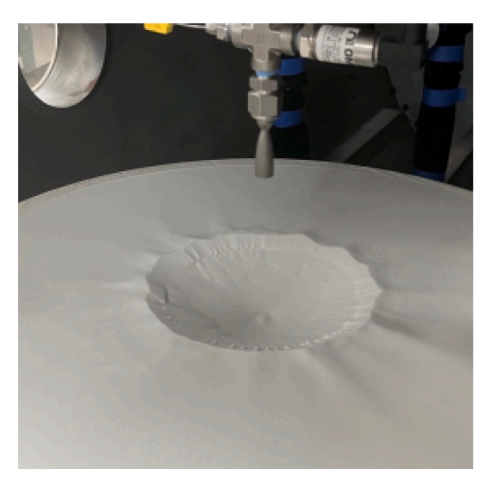


Fig. 14. Crater and ejecta tracking techniques developed by Silwal et al. [88] involving stereo-photogrammetry and particle tracking velocimetry.



(a) Interferometry apparatus containing radar and reflectors.



(b) Still frame used for crater evaluation post cratering.

 $\textbf{Fig. 15.} \ \ \textbf{Millimetre-wave interferometry setup for dust cloud characterisation by Rasmont et al. \ [92].}$

performed proof-of-concept atmospheric experiments using crushed walnut shells as Martian regolith simulant [67,96], where edge detection algorithms were tested to delimit the region of influence of the dust cloud. Moreover, particle image velocimetry (PIV) and laser Doppler anemometry (LDA) were implemented to characterise plume and dust cloud velocities. Takahiro et al. [97] carried tests with glass microspheres and varying nozzle pressure ratios, investigating flow behaviour through Schlieren imaging and tracking particle ejecta through PIV.

In 2024, Metzger [62,63] published a new lunar erosion theory that contradicted the viscous erosion theory developed by Roberts in 1963 [28]. He stated that soil erosion was not caused by a developing boundary layer and consequent shear stresses, but instead, by the gas flow energy diffusing into the soil, overcoming the grains potential energy, lifting them and accelerating them with the remaining horizontal kinetic energy. This theory was named the laminar sublayer energy flux theory and was supported by three lines of evidence from past experimental work, including field tests, crater growth tests and reduced gravity tests by the author and others. To partially verify the theory, Metzger revisited the Apollo landing videos and used the predicted optical density of blowing dust to estimate the erosion rate and the erosion efficiency, a newly defined parameter describing the fraction of flow energy converted into the mechanical energy lifting the grains. Through the integration of the erosion rate, the total eroded volume during the landing of Apollo 16 was estimated and found to be significantly greater than prior estimates, proving the significance and importance of plume-surface interactions in future missions.

3.3. Summary of test campaigns

Having carried out a chronological literature review of past PSI experimental work, the primary variables of each test campaign are collated in the following tables. Table 2 contains the experimental matrices: the gas or gases used in each experiment; exit flow variables including jet expansion ratio P_e/P_{atm} , exit Mach number M_e , and thrust T; impingement height h as a function of nozzle exit diameter d_e ; the lander represented by the scaled model where applicable; whether the plume was characterised (PC) prior to the introduction of regolith in the tests; and whether tests were performed in a reduced pressure environments (RPE). It should be noted that some of the non-dimensional values of P_e/P_{atm} and h/h_e in Table 2 have been calculated by the authors based on information provided in the papers to allow for a consistent comparison between experiments. Moreover, unit conversions for thrust have also been applied. Table 3 displays the materials used as regolith simulants, their particle size, and the justification for their choice. Lastly, Table 4 contains the erosion parameters measured and the apparatuses used.

4. Fundamental findings

Due to the focus placed by PSI researchers on erosion characterisation, the main findings of past studies have been related to the identification and classification of erosion mechanisms. Attempts at quantifying erosion properties of the different mechanisms have resulted in semi-empirical relationships, mostly applicable to viscous erosion. In this section, the five identified erosion mechanisms are described and their scaling relationships presented, as well as general findings on the effect of plume conditions on erosion.

4.1. Erosion mechanisms

4.1.1. Viscous shear erosion (VE)

Viscous shear erosion occurs when impinging flow is re-directed radially along the surface and develops a boundary layer, which induces a movement in the soil particles through viscous shear stress [41]. An analytical hypothetical theory was first developed by Roberts in

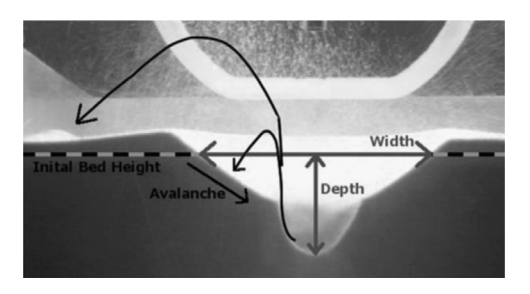


Fig. 16. Inner and outer crater formation arising from viscous erosion, from [58].

1963 [28], in which the mass erosion rate per unit area $\frac{dm}{dt}$ was assumed to be proportional to the difference between the gas shear stress τ^* and the soil shear strength, τ_0 :

$$\frac{1}{2}\theta u \frac{\mathrm{d}m}{\mathrm{d}t} = (\tau^* - \tau_0) = \Delta \tau \tag{1}$$

where u is the gas velocity and the product θu is the particle velocity, calculated using the fraction parameter θ , a function of particle diameter, gas variables, and thrust intensity, among others. In 2008, Eq. (1) was modified by Metzger et al. [53] to consider the ejection angle measured in Lunar landing videos, and to consider the particle size distribution of Lunar soil, as opposed to a unique particle size. However, almost two decades later, Metzger [62] declared Robert's theory invalid, claiming that lunar soil erosion is an energy flux phenomenon, where diffused gas flow introduces a net force under the grains and lifts them, exposing them to horizontal kinetic energy that displaces them. Although this represents a major disagreement with what was understood as viscous Lunar erosion up until 2024, it does not negate the scaling relationships that had been defined to date and are presented below, due to their empirical nature.

Viscous erosion is characterised by the formation of a parabolic inner crater and a conical outer crater, the latter appearing as a result of the avalanche of the steep sides of the inner crater and reaching an asymptotic crater size [51], shown in Fig. 16. The resulting outer crater has an inclination equal to the angle of repose of the particles.

Scaling with time

Experiments by Haehnel et al. [47] and Donahue et al. [48] revealed that high thrust levels caused an initial inner crater to form quickly before an outer crater appeared. On the other hand, low levels of thrust induced the simultaneous slow growth of both inner an outer craters. However, in both cases, cratering depth, d_c was found to vary logarithmically with time, t:

$$d_c = a\log(bt+1), t \ge 0 \tag{2}$$

where a and b are depth and time scaling parameters found experimentally. This implied that the excavation process was governed by the following equation:

$$dd_c/dt = abe^{-d/a} (3)$$

Parameter a was initially assumed to be a constant, but later work [51] proved that it was dependent on impingement height $(a \propto h)$; while b was observed to vary with gas density, ρ , impinging flow speed, u, jet exit plane, A and impingement height, h ($b \propto \rho u^2 A/h$). A relationship between crater volume, V and time was also presented:

$$V = \beta t^{\alpha} \tag{4}$$

where the scaling parameters β and α were calculated by finding a power law fit for the specific test case.

Scaling with particle size

Experiments by Metzger et al. [52] extended the dependency of a and b to include the effect of particle size d, finding that $a \propto d^{1/2}$ and $\beta \propto d^{-2}$. In 2010 [54], the effect of particle size on a was corrected to be $a \propto d^{1/3}$, such that $a^3 b \propto 1/d$.

 Table 2

 Experimental matrices of PSI experiments by various authors.

	es of PSI experiments by		M	h/d	T (NI)	Scaled lander	DC.	DDE
Experiment	Gas	P_e/P_{atm}	M _e	h/d_e	T (N)		PC	RPE
Land 1965 [30]	Ni	0–30	3.36	0–32		N/A	✓a	•
Land 1966 [31]	Не		2.68	1.05-9.32	8000–90 000	Lunar lander		~
Alexander et al. 1966 [34]	Ni	18.7–103		6.82–68.20	2890	Honest John spin rocket	✓b	
Mason 1969 [36]				1–8	5.34-444.82	Two engines		~
Clark 1970 [32]	Lqd prop ^c		4.53	0.28–3	445	LM of Apollo	✓b	~
Clark 1970 [40]	Не	4.39–10.3	4.21	21.8–528	19.5	Viking		~
Romine 1973 [41] Phase IA	Ni	1.42–1.47		10.46–26.4	667	Cold-gas nozzle	√ b	•
Romine 1973 [41] Phase II	Не			9.84–91.86	508.4–743.7	1/3 Viking	✓ b	~
Donahue 2005 [48]	He, Ni, Ar, CO2			8	"High & low thrust tests"		✓ ^d	
Haehnel 2008 [50]	Air		0.3					
Metzger 2008–2009 [51,52]	He, Ni, Ar, CO2		0.10-0.16 ^e	13.89–27.78				
Mehta 2010 [98]	Ni	0.9–4.3	7.32	34.5–50		1/4 Viking	✓b	~
Mehta 2011, 2013 [10,67]	NH3	3.7	4.8	8–60	160	1/2 Phoenix	✓f	~
Metzger 2011 [60]	O2, CH4				72			
Clark 2014 [22]	Ni			0.92–1.97				
LaMarche 2015 [58]	Air		0.03-0.28	6.5				
Metzger 2016 [69]	N2, He		0.14–1.46					~
Badr 2016 [70]	Ni		0.07	20–120			✓g	
Guleria 2020 [72]	Air		0.09–0.96	0.69–1.43			✓g	
Chambers 2020 [26] and Kuhns 2021 [73]	Air						✓b	~
Kuhns 2021 [73] (Terrestrial testing)	O2, CH4		6.06		448.8			
NASA's PFGT1 2022 [79,80,99, 100]	N2		5	3–13			✓h	~
Stubbs 2021–2022 [85,86]	Air	>1	1	25–70			√ i	
Stubbs 2023 [87]	Air	>1	1	4.6–37.1			✓ ^h	~
Rasmont 2022–2024 [90–92]	Ni	2.45–338	5	3–15	6.5		✓j	v
Gorman 2023 [81]			1 & 5.3	3-21.2				~

(continued on next page)

Table	2	(continued)	
rabie	7.	ссопппиеа і	

Subramanian 2024	Ni		6.6	4	øk	~
Silwal 2024 [88]	Air			9.3–55.6	V	~
Crane 2024 [89]	Air	1.34–2.03	≤1	25–50		

- ^a Shadowgraphs for shock standoff distances and surface pressure distribution at 8 h/d_e
- b Surface pressure distribution.
- ^c Hypergolic propellant, nitrogen tetroxide and a mixture of 50% hydrazine and 50% unsymmetrical dimethylhydrazine.
- d Controlled mass flow rates.
- e High velocities unspecified.
- f Impingement pressures of 3-22 kPa calculated based on the nozzle inlet stagnation pressures measured.
- g Mass flow rate measured during the experiments.
- h Flow variables monitored during experiments using static pressure transducers, thermocouples and vacuum gauges, sampled at 100 sps.
- i Schlieren flow visualisation.
- ^j Schlieren and surface pressures calculated in [102] for $h_{e} = 4 15$.
- ^k Growth of the plume expansion visualised using tracer particles.
- ¹ Static pressure and mass flow rate monitored during experiments.

Scaling with gravitational acceleration

Studies of PSI under reduced gravity from 2009 [52] concluded that a was only lightly affected by gravitational acceleration, g: $a \propto g^{-0.25}$, whilst the effect of gravitational acceleration on b was inconclusive.

Scaling with densimetric Froude number

In 1977, Rajaratnam and Beltaos [59] defined the erosion parameter E_c as a function of densimetric Froude number, F_r , exit diameter, d_e and impingement height, h:

$$E_c = F_r \frac{d_e}{h} \tag{5}$$

$$F_r = \frac{u}{\sqrt{g(\frac{\rho_p - \rho_f}{\rho_f})d}} = \frac{u}{\sqrt{g(\frac{\Delta_\rho}{\rho_f})d}}$$
(6)

where ρ_p is the intrinsic particle density and ρ_f is the fluid density. Eqs. (5) and (6) were used to estimate the asymptotic depth of a crater, D_{asym} :

$$\frac{D_{asym}}{h} = m_1 E_c + m_2 \tag{7}$$

where m_1 and m_2 are the slope and intercept parameters of the experimental linear fit, respectively. In 2015, LaMarche et al. [58] modified the Froude number to incorporate a function of particle shape, ϕ :

$$F_{r\phi} = \frac{u}{\sqrt{g(\frac{\Delta_{\rho}}{\rho_{f}})\phi d}} \tag{8}$$

In 2010, Metzger et al. [54] established that in the continuum regime, the volumetric erosion growth rate, \dot{V} was a function of the square of the densimetric Froude number, $F_r = \frac{u}{\sqrt{gd}}$:

$$\dot{V} \propto a^3 b \propto \frac{\rho_f u^2 D^2}{\rho_p g d} \propto F_r^2 \tag{9}$$

This equation was re-written in 2016 [69] as:

$$\dot{V} = BA \frac{\rho u^2}{\rho_m g \bar{d}} = BA F_r^2 \tag{10}$$

where B is a constant with units of velocity, not yet fully characterised, A is the jet exit area, and \bar{d} is the mean sand grain diameter.

In 2024, a volumetric growth was defined by the same author [62] to consider the angle of repose of the grains ϕ :

$$\dot{V} = \frac{\pi}{3} \cot^2 \phi \frac{\mathrm{d}d_s^2}{\mathrm{d}t} \tag{11}$$

Moreover, a new mass erosion rate *m* equation was also defined following the newly hypothesised laminar sublayer energy flux theory for soil erosion:

$$\dot{m} = \rho_b \frac{\varepsilon(E - E_{th})}{\rho_b g\langle D \rangle + \alpha} \tag{12}$$

where ρ_b is the bulk density of the soil, ϵ is a proportionality constant indicating the fraction of influx energy converted to mechanical energy (overcoming the grains potential energy), g is the gravitational acceleration, $\langle D \rangle$ is the mean particle diameter of grains and α is a gravity scaling constant. E is the downward energy flux from the gas, defined as:

$$\frac{1}{12}\rho_o v_o^2 \bar{v_T} \tag{13}$$

where ρ_o, v_o are the local gas density and velocity of the flow and \bar{v}_t is the mean thermal velocity of gas molecules. If $E > E_{th}$ erosion will occur, defining E_{th} as the thresholding value to initialise erosion.

Scaling with Knudsen number

In low-pressure experiments, Metzger et al. [69] attempted to incorporate a Knudsen number function, f(Kn) into Eq. (10):

$$Kn = \frac{\lambda}{r} \text{ where } \lambda = \frac{k_B T}{\sqrt{2\pi\sigma^2 P_o}}$$
 (14)

where r is the radius of sand grains, λ is the mean free path length of the jet gas molecules, k_B is the Boltzmann's constant, T is the jet temperature, σ is the collision diameter, and P_o is the jet static pressure. The experimental results did not allow for a single scaling factor to be defined, and it was concluded that scaling could be a function of multiple Knudsen numbers, with exit diameter or boundary layer thickness as the representative length scales.

The empirical relationships presented in Eqs. (1) to (14) have been defined by individual researchers, where the values for the required constants have been estimated for the specific test cases. However, a systematic corroboration of these relationships has not yet been carried out, or confirmed through real-world data. Only certain tendencies have been confirmed by independent researchers, just as the logarithmic crater growth with time, first described in 2005 [48] and recently observed in 2021 [85].

4.1.2. Explosive failure cratering/bearing capacity failure (BCF)

First identified by Alexander et al. in 1966 [34], explosive failure cratering or bearing capacity failure (BCF) is an erosion mechanism characterised by a sudden and rapidly-progressing through-depth erosion process, arising from an applied normal pressure that exceeds the bearing capacity of the soil. The model developed for this mechanism

Table 3

Experiment	Materials tested (diameter)	Justification	
Land et al. 1965 [30]	Aluminium oxide, pumice and sand (1–550 μ m).	Aluminium oxide is an abrasive material, relatively inert and available in closely graded sizes. Pumice is a porous volcanic glass with a fibrous structure with needle-like shapes.	
Land et al. 1966 [31]	Gravel and glass beads (70–1300 μm).	Glass beads are spherical and amenable to theoretical treatment. No justification provided for the use of gravel.	
Alexander et al. 1966 [34]	Sand, escalped earth (clay and silt) and sod soils (0.001–1.1 mm).		
Mason et al. 1969 [36]	Particulate material: 25% screened cinder, 50% sand, 25% pumice (0.03–2 mm).	Values for cohesion and angle of internal friction within range of lunar soil. Priority given to large-particle size range over duplicating the lunar particle size.	
Clark et al. 1970 [32]	Particulate material: 25% lava cinders, 50% crushed sandstone and 25% pumice (0.03-5 mm).	Lunar soil simulant (non-cohesive).	
Clark et al. 1970 [40]	Solid glass beads (0.15 mm).		
Romine et al. 1973 [41]	Lunar nominal soil (50 $\mu m)$ and volcanic sand (580 $\mu m).$	Volcanic sand has a particle size distribution from $<\mu m$ size particles to a very coarse fraction.	
Donahue et al. 2005 [48]	Quartz sand with a small fraction of muscovite (180–200 $\mu m).$		
Metzger et al. 2008–2009 [51,52]	Sieved quartz construction sand and JSC-Mars 1A (200–600 $\mu m).$	Sand is dry and cohesionless and JSC-Mars 1A is a Martian regolith simulant.	
Haehnel 2008 [50]	Glass beads (134 μ m), Ottawa sand (560 μ m) and polypropylene (6000 μ m).	Wide range of particles sizes selected to investigate the effect of permeability.	
Mehta et al. 2010 [98]	Ground walnut shells (100 and 1000 μm).	Contains 1/3 the density of Mars silica to match the 1/3 gravity Mars ballistic coefficient and particle trajectories.	
Mehta et al. 2011, 2013 [10,67]	Ground walnut shells (poorly sorted fine dust 160 μm , fine silt < 15 μm , and large coarse sand 850–2500 μm).	Sieved to resemble the size distributions of Martian basaltic sand.	
Metzger et al. 2011 [60]	Fine-grained volcanic tephra.	Present at experimental site and dust fraction within range of lunar soil.	
Clark 2014 [22]	Earth-source red sand (1 mm), JSC-1 lunar simulant (0.01–2 mm) and JSC Mars-1 (0.02–1 mm)		
LaMarche 2015 [58]	Plastic, glass and steel spheres, crushed glass, aluminium oxide and olivine (0.25–2.3 mm).	Smooth and angular particles selected to investigate the effect of shape on crater formation.	
Metzger 2016 [69]	"Play sand" (353.3 μm), glass beads (214.8 μm), plastic beads (798.2 μm), walnut shells (741.9 μm), corn cob 1027 μm), aluminium oxide (182.4 μm), quartz sand (151.5–473.1 μm) and JSC-1 Lunar simulant (87.8 μm).	Wide range of particle sizes selected to investigate the effect of Knudsen number.	
Badr 2016 [70]	Glass beads (200–300 µm).		
Guleria 2020 [72]	Mono and poly-dispersed glass beads (1-5 mm).	Range of sizes selected to investigate their effect on crater shape.	
Chambers 2020 [26] and Kuhns 2021 [73]	Steel beads (2 mm), glass beads (650–800 $\mu m)$, CI simulant and sand (150–250 $\mu m).$	Wide range of particle densities to investigate the effect of gravity. CI Orgueil is asteroid regolith simulant of the CI1 chondritic meteorite.	
Kuhns 2021 [73] (Terrestrial testing)	Volcanic red scoria fines (1–425 μm).	Found at a quarry in Arizona.	
NASA's PFGT1 2022 [79,80,99,100]	Mono-disperse (125–177 μ m) and bi-disperse sand (45–53 μ m and 125–177 μ m), tri-disperse mix (45–53 μ m, 125–177 μ m and 250–350 μ m), full range lunar (36–594 μ m), irregular mixture (212–350 μ m) and mono-disperse glass beads (125–177 μ m).	Mono-disperse silica sand is most similar to Martian regol and the BP-1 is most similar to Lunar regolith. Increasing complex simulants used for model validation and analysis PSI quantities of interest.	
Stubbs 2021–2023 [85–87], Silwal 2024 [88] & Crane 2024 [89]	Nearly pure quartz sand particles (600–850 μm).	Material selected as lunar simulant for its availability, cost and having been used in previous experiments. Particle size selected to limit the impediment of optical access.	
Rasmont 2022–2024 [90–92]	Ballotini glass microspheres (105 μ m).	Particles with a relatively narrow size distribution selected to simplify the PSI physics in the experiment and the calibration.	
Gorman 2023 [81]	Mono-dispersed sand and glass beads, bi-dispersed sand, and tri-dispersed sand (dimensions as specified above for [99]).	As in NASA's PFGT1 [99] shown above.	
Subramanian 2024 [101]	Glass microspheres: 3 M K46 (40 $\mu m)$ and 3 M K1 (65 $\mu m).$	Although not representative of lunar regolith shape, glass microspheres selected for their low density, varying cohesion, and are heat resistant.	

assumed a quasi-static phenomena where the surface load instantaneously matched the soil's internal stresses. The soil's shearing and inertial resistances were considered in combination with Coulomb,

Poiseuille, Laplace and Bossinesq's equations to model penetration depth and cratering radius. Formulae for maximum crater depth d_{max} and maximum radius of the surface r_{max} were defined as follows:

Table 4
Erosion parameters measured and apparatuses used in various PSI experiments.

Experiment	Crater depth or radius	Crater profile	Erosion rate	Erosion volume	Apparatuses
Land 1965 [30] Land 1966 [31]	<i>V</i>	<i>V</i>	<i>V</i>		X-ray, high-speed camera and sequence camera. X- ray.
Alexander 1966 [34]	·	·	·		High-speed camera (1000 fs).
Mason 1965 [36]	•	~		~	Not specified, external experiments.
Clark 1970 [40]	V			V	High-speed camera (400 fps), erosion computed by approximating spherical segments.
Romine 1973 [41]	V			V	Flat pressure plate, colour-coded striped stake network and coloured layers, high-speed photography and stereo-photography.
Donahue 2005 [48]	V	V		~	High-speed camera and machine vision software algorithms (100 fs).
Haehnel 2008 [50]	V	V			Bevelled edge, digital camera and MATLAB's Image Processing Toolbox.
Metzger 2009 [52,103]	V	V		V	Coloured sand layers and bisected experiments with high-speed videography and high-resolution videography.
Metzger 2010 [54] Mehta 2011 [67]	V	<i>V</i>	<i>V</i>		Bisected experiments, high-speed videography. Bisected experiments, high-speed videography, particle tracking.
Clark 2014 [22]	✓	~			Quasi-two-dimensional setup, high-speed videography.
LaMarche 2015 [58]	✓	~			High dynamic range camera (48 fps).
Metzger 2016 [69]		~	~	~	Videography.
Badr 2016 [70]	V	<i>.</i>			Profilometer.
Guleria 2020 [72]	<i>'</i>	~			High-speed camera and a monochrome sensor.
Chambers 2020 [26] and Kuhns 2021 [73]	V	~		•	Two cameras in stereo mode, GoPro and EKEN (240 fps).
Kuhns 2021 [73] (Terrestrial testing)	V		~		Still and high-speed cameras (1000 fs), thermocouples and pressure transducers buried in simulant.
NASA's PFGT1 2022 [79,80,99,100]	V	V			High-speed cameras (0.1-775 kHz frame rate).
Stubbs 2021–2023 [85–87]	V	V	~	V	Two high-speed stereo cameras (1000 fs).
Rasmont 2022–2024 [90–92]	V	V	V	V	Millimetre wave interferometry used to estimate dust cloud particle concentration & Azure Kinect 3D scanner and RecFusion software to estimate crater variables.
Gorman 2023 [81]	V	✓	V		Three high-speed cameras.
Subramanian 2024 [101]					Particle image velocimetry used to calculate ejecta speeds (double-pulsed laser and high-speed videography).
Silwal 2024 [88]					Two high-speed stereo cameras (1000 fps), and a laser sheet and high-speed camera (2000–4000 fps) for ejecta tracking.

$$d_{max} = 0.475 \sqrt{\frac{q_{ult}}{c}} \tag{15}$$

$$r_{max} = 0.62 \sqrt{\frac{q_{ult}}{\sqrt{2\pi}c}} \tag{16}$$

where q_{ult} is the bearing capacity of the soil and c is the cohesive strength of the soil. It should be noted that bearing capacity failure was initially considered to be an unlikely erosion process during a Lunar landing, due to the high relative density and shear strength of Lunar soil [51]. However, the thrusters of future landers will induce forces on the soil much greater than ever experienced, removing bulk quantities of soil which could potentially change its properties or expose deeper areas where discrete varying densities might be present. This terrain modification stage was discussed by Metzger et al. [60] in 2011, and could lead to the presence of explosive cratering, even on the Moon.

4.1.3. Diffused gas eruption (DGE)

Diffused gas eruption is characterised by a single eruption event after engine shut-down or by an annular ring during firing. In Scott and Ko's experiments of 1969 [35], it was identified that impinging flow was not only re-directed by the surface, but could also diffuse into the surface and exit normal to the surface at a radial offset location. Hence, assuming that the surface is a porous medium, the throughdepth trajectory of the flow was modelled via Darcy's Law [104]:

$$\nabla^2 p^2 = (2n\mu/k)(\partial p/\partial t) \tag{17}$$

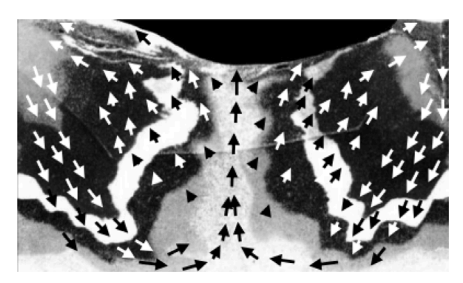
where p is the impinging pressure, n is the porosity of the medium, μ is the viscosity of the gas, and k is the permeability of the medium to gas flow. Through mathematical manipulations of Eq. (17) (see [35]), a set of curves were computed, relating the pressures at a given depth and radial positions with time. These allow the direction of flow to be inferred by observing the pressure gradients, as well as the body forces on the soil. It was concluded that when the vertical force exceeds the weight of the soil, an instability may occur and soil can be lifted upwards, depending on its cohesion. Gas diffusion and soil instabilities were modelled by Chambers et al. [71] following Darcy's Law, with the objective of quantifying the risk of NASA's Asteroid Redirection Mission.

4.1.4. Diffusion-driven flow (DDF)

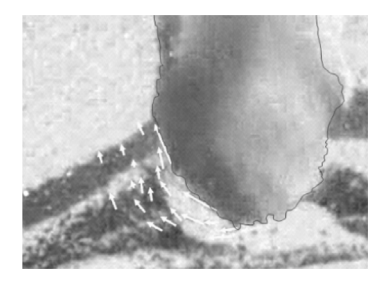
As with diffused gas eruption, diffusion-driven flow is an erosion mechanism that requires the soil to be permeable. However, diffusion-driven flow occurs deep beneath the surface, where shearing forces tangential to the forming cavity displace the soil, allowing the crater to grow. This mechanism was observed in bisected experiments in 2008 [51], where coloured layers allowed the tangential movement of sand particles to be identified, shown in Fig. 17. To the best of the author's knowledge, no analytical theories have been developed to explain this behaviour.

4.1.5. Diffusive gas explosive erosion (DGEE)

Discovered by Mehta [17], diffusive gas explosive erosion is the dominating process when supersonic pulsed jets impinge on porous soil.



(a) Cross-section of sand after cratering.



(b) Still frame showing tangential movement of particles around crater.

Fig. 17. Recorded crater development by Meztger et al. in 2008 [51].

The characteristic cyclic loading, and hence the pressure variations, cause the gases to penetrate into and diffuse outwards from the soil, causing fluidisation of the surface. This induces variations in soil porosity and, as a result, variations in the granular speed of sound. Hence, the large pressure gradients from the pulsation of jets cause shock waves to appear and propagate in regions of reduced acoustic velocity. These processes are termed cyclic granular shock waves and have the ability to remove substantial quantities of soil in a short period of time. It was found experimentally that the crater growth rate found in pulsed jets (and hence caused by DGEE) was five times greater than that found in steady jets (caused by BCF or DDF). In 2020, Chambers [26] observed on-centre re-eruption, which was attributed to be a single pulse case of diffusive gas explosive eruption.

4.2. General relationships

Although viscous erosion is the mechanism that has been more extensively quantified, general relationships between impinging conditions and the resulting erosion have been established through experimental observation, independent of the predominant mechanism present. Erosion volume increases with jetting time [26] and decreases with increasing descent speed [36], and has been found to be proportional to thrust intensity and inversely proportional to the square root of impingement height [36]. Moreover, reducing impingement height increases normal impingement pressure and surface heating [32], leading to an increase in ejecta mass and angle [26]. Ejection angle has also been found to vary with thrust, as observed in the dust ejection angle variations between sequential frames of the Apollo 12 landing videos [39]. Erosion characteristics were also found to be a function of the surface materials, with increased cohesion decreasing erosion [31] and ejecta volume [26]. Moreover, increasing the particle size of the soil also results in an increased erosion [17,31]. In terms of the asymptotic erosion state, craters forming in a surface with larger particles have been found to reach an asymptotic size faster than in a surface with smaller particles [58].

5. Challenges of experimental PSI

The challenges associated with the design and performance of PSI experiments are presented below, divided into representative environments, regolith simulants, diagnostic techniques, current procedures and experimental consistency, and lack of mission data.

5.1. Representative environments

Extra-terrestrial environments are often termed extreme environments due to the presence of life-threatening conditions such as radiation, plasma, vacuum, high variations in temperature, or microgravity. In order for terrestrial experiments to be representative of these environments, it is imperative that some of the conditions are recreated; mainly, the reduced pressure and microgravity for PSI experiments.

To achieve the first, vacuum chambers are used, where the ambient pressure is decreased to sub-atmospheric levels. These facilities require a significant amount of time to pump down (of the order of 4 h for a 12 m³ test section to reach Martian pressure), which limits the number of tests which can be performed in a day. Moreover, during pump down, outgassing occurs where air molecules trapped in the simulant are released. This disturbs the surface, which can affect the soil's compaction and surface homogeneity. Lastly, maintaining a constant background pressure in the test section is difficult due to the added mass flow by the firing jets. To overcome this, ballast chambers and control valves are used, which increase the total volume of vacuum available and allow the background pressure to be maintained. However, the performance of valves, pumps and seals can be affected by the presence of abrasive regolith simulants, decreasing the ability to maintain a constant vacuum level.

With regards to microgravity, it can be simulated via two approaches: performing experiments in drop towers or parabolic flights, or selecting regolith simulants with densities to match the gravitational force in reduced gravity environments [98]. Lastly, the generated plumes must also be representative of the retro-propulsion rockets used in landers, in terms of thrust intensity or non-dimensional parameters such as Mach number, Froude number or Reynolds number [17].

5.2. Regolith simulants

The surface particles found on the Moon, Mars, or on asteroids, can vary greatly in chemical, mechanical and aerodynamic properties, and are substantially different to particles present on Earth. Lunar dust, for example, has never been exposed to hydrological and aeolian erosion, causing it to have very sharp edges, a hardness 50% higher than steel alloys, and to be electrostatically loaded [8]. It is evident that the choice of regolith simulants in PSI experiments will be dependent on the environment to be represented, and also on the regolith properties with most impact on the problem examined. If a given test is intended to study the contamination of the plumes on the surface, the chemical properties of regolith will be matched (for example, by selecting the JSC-1/1A simulant in a Lunar experiment). Conversely, if erosion mechanisms or ejecta speeds are to be analysed, properties that affect particle trajectories such as cohesion or microgravity will be prioritised (for example, by using crushed walnut shells in Martian experiments [93]). It should be noted, however, that a consistent scaling of granular material is very difficult, as particle size has an effect on cohesion, drag force, mass and permeability.

As shown in Table 3, in PSI experimental work, a wide range of simulants have been used in studies recreating the same environments, which hinders a like-for-like comparison of the results. The choice of simulant is not only dependent on the regolith properties that are to be prioritised, but also on availability and cost. Institutions such as the Lunar Surface Innovation Consortium (LSIC) perform geotechnical assessments of regolith simulants [105], in order to compare and evaluate the available options and provide guidance on their use in experimental work.

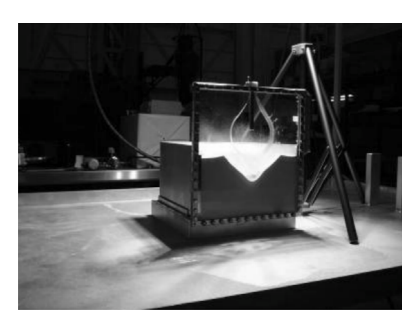


Fig. 18. Half-plane cratering apparatus by Metzger et al. in 2008 [51].

Although there are many simulants with quantified properties, the effect of the choice of simulant on a PSI experiment is still unknown. By prioritising certain properties, part of the physics involved might be neglected, which could have an impact on the validity of conclusions drawn, emphasising once again the challenges of this field of research.

5.3. Diagnostic techniques

The characterisation of plume-surface interactions can be divided into two parts: the analysis of the plume, and the quantification of the resulting crater development, ejection of particles, and formation of the dust cloud. In low-pressure environments, the analysis of plume structures and conditions is particularly challenging, as traditional flow visualisation techniques such as Schlieren or Shadowgraph photography are not effective, given that density variations in a near-vacuum are not substantial enough to be captured. Background-oriented Schlieren (BOS), which uses a dotted pattern background and correlation techniques [106], was developed to mitigate this, but its capability is still limited. Other alternatives for low-pressure environment flow visualisation include planar laser-induced fluorescence (PLIF), which uses the fluorescence resulting from electronic excitation of nitric oxide to highlight flow structures such as shocks or shear layers [83]. To date, nozzle flows in PSI experiments have been mainly characterised in terms of their exit conditions and impingement pressures, through pressure transducer plates, pressure sensitive paints (PSP), or buried pressure transducers for sub-surface pressure measurements [73]. Surface shear stresses have also been estimated, mostly by the measurement of velocities using pitot tubes [76] and hot-film anemometers [107]. With regards to the quantification of erosion, a number of techniques have been explored, presented in the following section, along with their main advantages and limitations.

5.3.1. Bisected configurations

Using a splitter plane and a transparent viewing pane, half-plane two-dimensional experiments can be carried out (shown in Fig. 18), in which sub-surface particle movement can be observed. Using high-speed videography, both ejecta particles and crater development can be recorded, including the sub-surface behaviour which would otherwise be hidden. The main limitation of this approach, however, is the introduction of an intrusive artificial boundary on the regolith bed, as well as the modification of the plume, caused by deviating nozzle exit flow away from the test section using the splitter (as shown in Fig. 19).

5.3.2. Stereo-photogrammetry

Stereo-photogrammetry consists of the combination of images taken at different perspectives to obtain a three-dimensional reconstruction of an object. In PSI experiments, this principle can be used to measure the dynamic crater formation process in a non-intrusive manner [87]. This requires optical access to the crater, which can become challenging if a dense cloud of particles forms ahead of the cameras. As seen in the footage of landing spacecraft, the obstruction of cameras

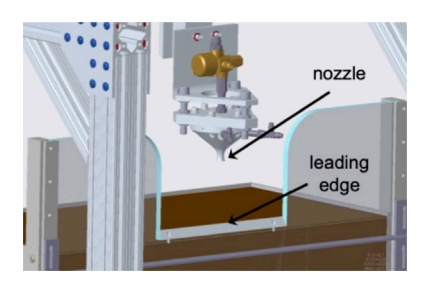


Fig. 19. Splitter plate leading edge used in NASA's PFGT campaign in 2022 [78].

is highly probable, which will inevitably limit the use of onboard stereo-photogrammetry. Figs. 20(a) and 20(b) show a stereo-camera PSI facility developed by Stubbs et al. [87], and the crater reconstruction achieved.

5.3.3. Particle image velocimetry

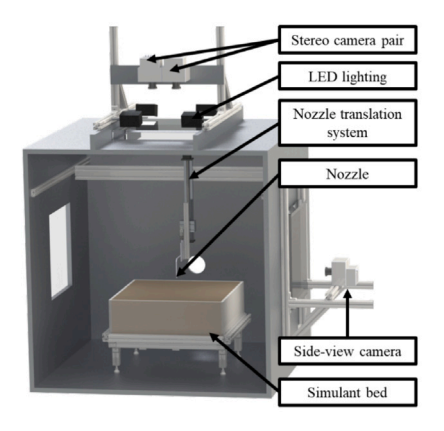
Particle image velocimetry (PIV) is a technique that allows the velocity field of a region to be measured instantaneously. A pulsating laser is used to illuminate the region of interest while a synchronised camera captures image pairs. Tracking particles are introduced into the test section, a process known as seeding, and through the correlation of image pairs, the local velocities of the flow are estimated. In PSI experiments, PIV has recently been applied to measure the speeds of ejected particles. In this approach, no external seeding is introduced in the tests, and instead, the regolith particles act as tracers themselves, as the variable of interest is ejecta speeds rather than flow speed. The main challenge of PIV in gas-granular experiments is over-saturation: when the plume first impinges on the surface, a great quantity of particles are lofted, which can cause too much light to be reflected and saturate the image, impeding the visualisation of individual in the image pairs. Although non-intrusive, this technique requires a laser to illuminate a plane, which introduces a spatial filter and results in the velocity field measured to be two-dimensional. Moreover, there is a risk of misscorrelation of suspended particles occurring between recorded frames, which would still provide a velocity field, although incorrect.

5.3.4. Radar tomographic interferometry

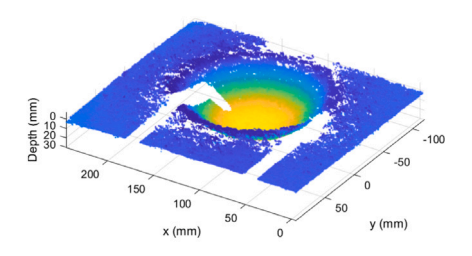
Radar interferometry is based on the principle that the presence of particles in a medium will modify its dielectric properties, and, in turn, the propagation speed of a signal. Through the use of a radar and a reflector (shown in Fig. 21), the time-of-flight of a signal can be measured, and through the phase shift comparison between a signal propagating in a particle-mixture and a signal propagating in a homogeneous medium, the volume fraction of particles can be estimated [90]. Moreover, if signal reflectors are placed around a region of interest, a tomographic reconstruction can be achieved, in which the local particle concentrations are derived from a sparse set of path-integrated measurements [92], as shown in Fig. 22. Applied to PSI experiments, radar tomographic interferometry can be used to estimate the particle concentrations of the dust cloud that results from plume impingement. However, this requires the dielectric properties of the regolith particles to be known, or a calibration process to be performed in order for the interferometric variables of the dust cloud to be estimated. This becomes particularly challenging if particles of different sizes are present, which is indeed the case for extra-terrestrial plume-surface interactions.

5.4. Profilometry

Profilometry is a technique that measures the local topography of a region, establishing its variation in surfaces along one or more directions. Profilometers can be of two types: a stylus, which physically moves to probe the surface, or an optical profilometer, which uses



(a) Stereo-camera apparatus.



(b) Crater reconstruction.

Fig. 20. Stereo-photogrammetry setup and post-processing by Stubbs et al. in 2023 [87].

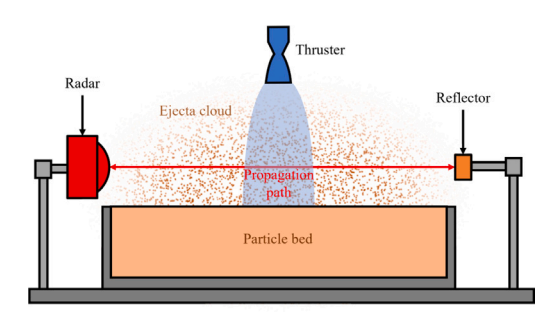


Fig. 21. Diagram of radar interferometry setup by Rasmont et al. in 2023 [91].

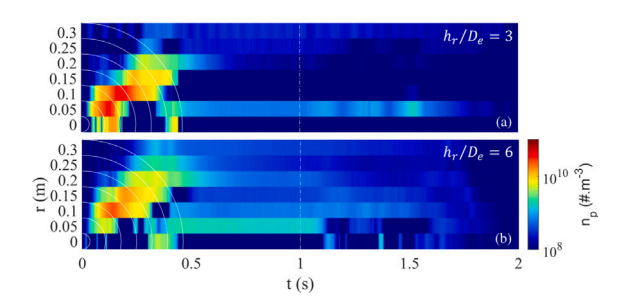


Fig. 22. Concentration of ejection as a function of radial location measured using interferometry by Rasmont et al. in 2024 [92].

the direction and detection of light to infer the surface roughness. In experiments carried out by Badr et al. [70], a laser profilometer was used to measure the shape of the crater resulting from plume impingement. This technique, although non-intrusive, can only be used to measure the crater shape after the cratering event has finished, as throughout its development, ejecta particles would interfere with the laser path.

5.5. Current procedures and experimental consistency

Since the 1960s, PSI experiments have followed a similar procedure: preparation of regolith beds, pump down of vacuum chambers where applicable, firing of nozzles, and recording of erosion and ejecta through high-speed videography and/or other diagnostic techniques. However, even though procedures have not varied significantly, Tables 2 to 4 show the lack of consistency between experiments, in terms of regolith simulants used, the properties of the plumes, impingement heights tested and erosion parameters measured. Moreover, there is very limited information on the repeatability of these experiments, such

as the number of tests performed per campaign and their statistical reliability, the procedures followed for regolith re-setting to ensure homogeneity and avoid compaction, or the measures taken to account for changes in ambient temperature or moisture during a campaign and their effect on regolith behaviour. The only published guidance on PSI experiments is NASA's 1008 Technical Standard: Classification and requirements for testing systems and hardware to be exposed to dust in planetary environments [108]. Although the document mainly focuses on Lunar dust guidelines such as sourcing of simulants or impact assessment processes, it also contains a brief section on PSI testing. In this section, best practices are stated, including that the regolith bed depth should exceed the plumes' penetration distance, or that the test area should be greater than the area of PSI effect. It also contains factors to consider in the design of experiments, such as pressure or microgravity, as discussed in the previous sections.

5.6. Mission data

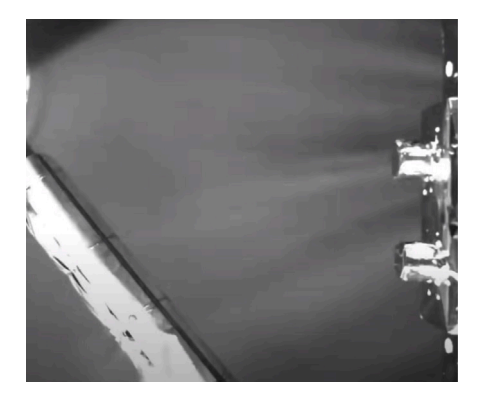
The field of PSI was first established when the Apollo landing videos showed the surface disturbance and dust ejection caused by the impingement of retro-propulsive rocket plumes. The footage was later used to estimate ejection angles [39] and Lunar dust transport [61], and remains to date one the few mission data sets available on which quantitative conclusions can be drawn. In recent missions, the impact of PSI has been observed, such as the obstruction of onboard cameras of the Chang'e 4 (as shown in Fig. 23) and the visual recorded data has been used to infer quantitative information [109].

To increase the availability of real-scenario PSI data, and hence verify numerical models or terrestrial experiments, future missions will be equipped with systems able to record surface development during landings. In February of 2024, Intuitive Machine's Nova-C lander was equipped with an EagleCam and four Stereo Cameras for Lunar Plume-Surface Studies (SCALPSS). The EagleCam, a cubesat camera system developed by Embry-Riddle University, was designed to capture the first third-person views of a Lunar lander [110]. However, after an unexpected landing resulting in a tilting of the spacecraft, the camera was ejected but no data was received by the lander. The SCALPSS cameras, planned to provide a coverage and a three-dimensional reconstruction of 84% of the surface below the lander [111-113], experienced poweron and triggering issues due to the faster-than-expected descent, but successfully recorded thumbnail images. SCALPSS is planned to be on board Firefly Aerospace's Blue Ghost Lander and Blue Origin's MK1 cargo lander [114].

In addition to videographic instruments, other optical systems include the EJECTA storm instrument, which uses lasers and the measurement of transmitted and back-scattered light to estimate the particle size distribution of travelling dust clouds [74]; the GrainCams, two



(a) Surface of the Moon is visible.



(b) Lofted dust obstructs the surface.

Fig. 23. Onboard camera footage of Chang'e 4 landing. Credits: China National Space Administration (CNSA)

optical rover-mounted instruments (SurfCam and LevCam) designed to observe lunar soil and levitating particles on the lunar surface [115]; and the work by Peale et al. [116,117] on a laser propagation decay system to calculate particle size distributions in ejecta plumes during the final stages of landing.

Radar-based techniques are also being developed to capture realtime PSI, such as the Dust Ejecta Radar Technology (DERT) [118,119], which uses a millimetre wave doppler radar and the recorded shifted frequency of ejected particles to estimate their velocity. Lastly, with regards to ejecta energy measurements and damage predictions, the particle impact event (PIE) sensor is being designed to measure the kinetic energy and flux of ejecta during landing [120].

6. Conclusions from experimental work and recommendations

As we plan our imminent returns to the Moon and target to send crewed missions to Mars by the 2030s [121], it is essential that the safe return of astronauts is ensured. To achieve this, an understanding of the physics involved in one of the most important and crucial phases during landing must be achieved, namely, of those present in the plume-surface interactions (PSI) occurring in the last metres of powered descent. These phenomena can have severe detrimental effects on spacecraft, such as damage of hardware and loss of stability. Moreover, these effects are expected to scale with spacecraft mass [6] and considering that planned missions will be significantly heavier than those of the Apollo era, it is imperative that PSI are accounted for in mission design and planning.

In the last sixty years, a wide range of experimental work has been carried out in the field of PSI, both under ambient conditions and in reduced pressure environments. Through the observation of crater development, five erosion mechanisms have been identified: viscous erosion (VE), bearing capacity failure (BCF), diffusion-driven flow (DDF), diffused gas eruption (DGE), and diffusive gas explosive eruption (DGGE). Scaling relationships have been developed for VE; estimates for maximum crater dimensions have been formulated for BCF, and governing equations have been suggested for DGE. However, a complete understanding of all erosion mechanisms has not been achieved, and neither the boundaries or potential interactions between them. Hence, further work is required in the analysis of erosion resulting from plume impingement, in order to better predict particle ejection and estimate their damaging capability.

Due to the lack of real-world data sets, many findings from experimental work have not been confirmed, and numerical models have not been validated. Experimental work has lacked a true representation of the environmental conditions encountered during Lunar and Martian landings. For that reason, all future missions should be equipped with systems able to record relevant PSI data, especially considering the growing interest of sustained presence on the Moon. Determining safe

distances between Lunar habitats and landing sites of spacecraft will be achieved through a combination of experimental and numerical work and learnt lessons from successful landings. Plume and surface monitoring payloads are therefore essential.

While mission data is not yet available, Computational Fluid Dynamic (CFD) solvers can be partially validated by experimental work. If experiments fully characterise the plumes tested, not just in terms of their nozzle exit properties, but in terms of the properties at the surface, the flow modelled in solvers could be verified before interacting with the particles. Moreover, it would allow the relationship between flow structure and erosion to be further explored. Although numerical models are invaluable for informing mission and spacecraft design for PSI resilience, these remain in their infancy and rely heavily on (often classical) experimental data and validation. Numerical work is beyond the scope of this review and has not been discussed further, as a thorough review of numerical simulation methodologies will be presented in a separate paper.

PSI is a highly complex problem involving the simultaneous presence of continuum and rarefied flow, and gas-granular interactions with particles of a range of sizes and properties. As discussed in Section 5, carrying out PSI experiments is extremely challenging due to the different conditions that must be recreated. Considering the huge parameter space involved in PSI, it is of the authors' opinion that upcoming experimental campaigns should be carried in a very controlled manner, in which tests begin in their simplest form and progressively increase their parameter space, in order to be able to assess the impact of different variables on erosion and ejecta, such as erosion rate and volume, and ejection angle and speeds.

To achieve this, campaigns need to fully characterise the plume conditions prior to the introduction of particles, in order to understand the forces and momentum induced by the jet and be able to relate them to the erosion processes occurring as a result. Stagnation pressure, exit pressure, exit velocity distribution, impingement pressure and impingement velocities should be measured, initially in cold flow experiments before expanding the experimental matrices to heated tests. With regards to the regolith simulants, their particle size and distributions must be quantified, and regolith handling and resetting procedures should be established to achieve consistent initial boundary conditions. This includes regolith bed compaction, surface roughness, homogeneity and distance from the jet exit. Moreover, environmental fluctuations between tests should be monitored, such as humidity, as the moisture in the regolith could have a significant effect on the initial bed conditions due to outgassing. A range of simulants should be used, to relate predominant particle variables with measured erosion.

It is also strongly recommended that recorded variables are verified by the use of redundant measurement techniques, and that are validated by collaborating research groups replicating test conditions, such that like-for-like results can be compared, which is one of the

fundamental gaps in past experimental work. In a similar manner, recently developed diagnostic techniques require benchmarking, essential to allow conclusions to be drawn from measured variables.

Mission environmental variables should be recreated in tests, such as reduced pressure by testing in dirty vacuum chambers or in drop towers for reduced gravity. However, the authors believe that atmospheric tests should still be carried out, as they provide a reduction in uncertainty that can allow for simpler cases to be benchmarked and diagnostic techniques to be matured prior to the study of more complex scenarios.

To conclude, although the fundamental physics of plume-surface interactions are still to be characterised, this field has recently drawn significant attention as indicated by the recent number of papers and research groups looking into PSI. Given the renewed interest in Lunar and Martian activities, a better understanding of PSI will not only support new missions, but be essential in their success.

CRediT authorship contribution statement

Claudia Jimenez Cuesta: Writing – review & editing, Writing – original draft, Conceptualization. Jack Davies: Writing – review & editing. Kevin Worrall: Writing – review & editing, Supervision. Andrea Cammarano: Writing – review & editing, Supervision. Hossein Zare-Behtash: Writing – review & editing, Supervision.

Declaration of competing interest

The authors declare that they have no known competing financial interests or personal relationships that could have appeared to influence the work reported in this paper.

Acknowledgements

This work is supported by the Mary Gibb Dunlop Endowment Fund of the School of Engineering at the University of Glasgow, United Kingdom.

References

- [1] K.T. Edquist, S.A. Scott, M.N. Rhode, B. Kelb, A. Korzun, A.A. Dyakonov, K.A. Zarchi, D.G. Schauerhamer, E.A. Post, Supersonic retropropulsion technology development in NASA's entry, descent, and landing project, in: 9th International Planetary Probe Workshop, 2012.
- [2] Y. Langevin, 10.17 mission analysis issues for planetary exploration missions, in: G. Schubert (Ed.), Treatise on Geophysics, Elsevier, 2007, pp. 565–593, http://dx.doi.org/10.1016/B978-044452748-6.00170-X.
- [3] P. Metzger, J.E. Lane, C.D. Immer, S. Clements, Cratering and blowing soil by rocket engines during lunar landings, in: International Conference on Case Histories in Geotechnical Engineering, 2008.
- [4] C. Immer, P. Metzger, P.E. Hintze, A. Nick, R. Horan, Apollo 12 lunar module exhaust plume impingement on lunar surveyor III, Icarus (ISSN: 0019-1035) 211 (2) (2011) 1089–1102, http://dx.doi.org/10.1016/j.icarus.2010.11.013.
- [5] J. Lane, S. Trigwell, P. Hintze, P. Metzger, Further analysis on the mystery of the surveyor III dust deposits, in: Earth & Space 2012, 2012.
- [6] P.T. Metzger, Dust transport and its effects due to landing spacecraft, in: Lunar Dust 2020, Lunar and Planetary Institute, 2020.
- [7] J.R. Gaier, The effects of lunar dust on EVA systems during the apollo missions, NASA Tech. Memo. (2007).
- [8] D. Budzyn, Implicit lunar dust mitigation technology: Compliant mechanisms, Acta Astronaut. (ISSN: 0094-5765) 203 (2023) 146–156, http://dx.doi.org/10. 1016/j.actaastro.2022.11.042.
- [9] spaceX, Starship overview, 2024, URL https://www.spacex.com/vehicles/ starship/.
- [10] M. Mehta, A. Sengupta, N.O. Renno, J.W. van Norman, P.G. Huseman, D.S. Gulick, M. Pokora, Thruster plume surface interactions: Applications for spacecraft landings on planetary bodies, AIAA J. 51 (12) (2013) 2800–2818, http://dx.doi.org/10.2514/1.J052408.
- [11] J. Capecelatro, Modeling high-speed gas-particle flows relevant to spacecraft landings, Int. J. Multiph. Flow (ISSN: 0301-9322) 150 (2022) 104008, http: //dx.doi.org/10.1016/j.ijmultiphaseflow.2022.104008.
- [12] J.D. Anderson, Modern Compressible Flow, Mc Graw Hill, 1982.

[13] C. Donaldson, R. Snedeker, A study of free jet impingement part 1, mean properties of free and impinging jets, J. Fluid Mech. 45 (2) (1971) 281–319, http://dx.doi.org/10.1017/S0022112071000053.

- [14] F. Duronio, C. Villante, A.D. Vita, Under-expanded jets in advanced propulsion systems;a review of latest theoretical and experimental research activities, Energies 16 (18) (2023) http://dx.doi.org/10.3390/en16186471.
- [15] A. Korzun, Aerodynamic and Performance Characterization of Supersonic Retropropulsion for Application to Planetary Entry and Descent, Georgia Institute of Technology, 2012.
- [16] J.C. Carling, B.L. Hunt, The near wall jet of a normally impinging, uniform, axisymmetric, supersonic jet, J. Fluid Mech. 66 (1) (1974) 159–176, http://dx.doi.org/10.1017/S0022112074000127.
- [17] M. Mehta, Plume-Surface Interactions due to Spacecraft Landings and The Discovery of Water on Mars, University of Michigan Library, 2010.
- [18] M. Pindzola, Jet simulation in ground test facilities, AGARDograph 79 (1963).
- [19] D. Edgington-Mitchell, D.R. Honnery, J. Soria, The underexpanded jet mach disk and its associated shear layer, Phys. Fluids (ISSN: 1070-6631) 26 (9) (2014) http://dx.doi.org/10.1063/1.4894741.
- [20] NASA, Moon fact sheet, 2024, URL https://nssdc.gsfc.nasa.gov/planetary/factsheet/moonfact.html.
- [21] NASA, Mars fact sheet, 2024, URL https://nssdc.gsfc.nasa.gov/planetary/factsheet/marsfact.html.
- [22] A.H. Clark, R.P. Behringer, Jet-induced 2-D crater formation with horizontal symmetry breaking, Granul. Matter 16 (4) (2014) http://dx.doi.org/10.1007/ s10035-014-0501-9.
- [23] ESA, Highlands and mare landscapes on the moon, 2006, URL https://www.esa.int/Science_Exploration/Space_Science/SMART-1/Highlands_ and_Mare_landscapes_on_the_Moon.
- [24] M. Isachenkov, S. Chugunov, Z. Landsman, I. Akhatov, A. Metke, A. Tikhonov, I. Shishkovsky, Characterization of novel lunar highland and mare simulants for ISRU research applications, Icarus (ISSN: 0019-1035) 376 (2022) http://dx.doi.org/10.1016/j.icarus.2021.114873.
- [25] E. Grün, M. Horanyi, Z. Sternovsky, The lunar dust environment, Planet. Space Sci. (ISSN: 0032-0633) 59 (14) (2011) http://dx.doi.org/10.1016/j.pss.2011.04. 005
- [26] W. Chambers, Experimental and Computational Investigation of Plume Surface Interactions in Vacuum Microgravity, University of Central Florida, 2020.
- [27] Z. Cao, C.W.C. amd M.B. Agir, K. Kontis, Lunar plume-surface interactions using rarefiedMultiphaseFoam, Front. Mech. Eng. 9 (2023) http://dx.doi.org/ 10.3389/fmech.2023.1116330.
- [28] L. Roberts, The action of a hypersonic jet on a dusty layer, Inst. Aerosp. Sci. (1963).
- [29] L. Roberts, Exhaust jet dust layer interaction during a lunar landing, in: XIII International Astronautical Congress, 1964.
- [30] N.S. Land, H.F. Scholl, Experimental investigation of jet impingement on surfaces of fine particles in a vacuum environment, NASA Rep. (1965).
- [31] N.S. Land, H.F. Scholl, Scaled lunar module jet erosion experiments, NASA Rep. (1966).
- [32] L.V. Clark, Experimental investigation of close-range rocket-exhaust impingement on surfaces in a vacuum, NASA Rep. (1970).
- [33] L.E. Stitt, Interaction of Highly Underexpanded Jets with Simulated Lunar Surfaces, NASA Technical Note D-1095, 1961.
- [34] J.D. Alexander, W.M. Robers, R.F. Scott, Soil erosion by landing rockets final report, NASA Rep. (1966).
- [35] R.F. Scott, H.Y. Ko, Transient rocket-engine gas flow in soil, AIAA J. 6 (2) (1968) 258–264, http://dx.doi.org/10.2514/3.4487.
- [36] C.C. Mason, E.F. Nordmeyer, An empirically derived erosion law and its application to lunar module landing, GSA Bull. (ISSN: 0016-7606) 80 (9) (1969) 1783–1788, http://dx.doi.org/10.1130/0016-7606(1969)80[1783:AEDELA]2.0.
- [37] E. Christensen, R. Choate, L.D. Jaffe, R.L. Spencer, F.B. Sperling, S.A. Batterson, H.E. Benson, R.E. Hutton, R.H. Jones, H.Y. Ko, F.N. Schmidta, R.F. Scott, G.H. Sutton, Surveyor V: Lunar surface mechanical properties, Sci. New Ser. (1967) 637–640
- [38] R.F. Scott, Apollo program soil mechanics experiment: Final report, NASA Rep. (1975).
- [39] C. Immer, J. Lane, P.T. Metzger, S. Clements, Apollo video photogrammetry estimation of plume impingement effects, Icarus (ISSN: 0019-1035) 214 (1) (2008) 46–52, http://dx.doi.org/10.1016/j.icarus.2011.04.018.
- [40] L.V. Clark, Effect of retrorocket cant angle on ground erosion a scaled viking study, NASA Rep. (1970).
- [41] G. Romine, T.D. Reisert, J. Gliozzi, Site alteration effects from rocket exhaust impingment during a simulated viking mars landing, NASA Rep. (1973).
- [42] H.J. Moore, R.E. Hutton, R.F. Scott, C.R. Spitzer, R.W. Shorthill, Surface materials of the viking landing sites, J. Geophys. Res. 82–28 (1977).
- [43] R.E. Hutton, H.J. Moore, R.F. Scott, R.W. Shorthill, C.R. Spitzer, Surface erosion caused on mars from viking descent engine plume, Earth Moon Planets 23 (1980) 293–305, http://dx.doi.org/10.1007/BF00902045.
- [44] W.F. Carroll, Analysis of surveyor 3 material and photographs returned by apollo 12, NASA Rep. (1972).

- [45] L. Jaffe, Blowing of lunar soil by apollo 12: Surveyor 3 evidence, NASA Rep.
- [46] P. Metzger, T.V. Bruce, Rocket exhaust cratering: Lessons learned from viking and apollo, NASA Cent. Aerosp. Inf. (2004).
- [47] R.B. Haehnel, B. Cushman-Roisin, W.B. Dade, Cratering by a subsonic jet impinging on a bed of loose particles, in: Earth & Space 2006, 2006, pp. 1–8, http://dx.doi.org/10.1061/40830(188)19.
- [48] C.M. Donahue, P.T. Metzger, C.D. Immer, Empirical scaling laws of rocket exhaust cratering, in: 56th International Astronautical Congress, 2005.
- [49] N. Rajaratnam, Erosion by submerged circular jets, J. Hydraul. Div. (1982).
- [50] R.B. Haehnel, W.B. Dade, B. Cushman-Roisin, Crater evolution due to a jet impinging on a bed of loose particles, in: Earth & Space 2008, 2008, pp. 1–10, http://dx.doi.org/10.1061/40988(323)2.
- [51] P.T. Metzger, C.D. Immer, C.M. Donahue, B.M. Vu, R.C. Latta III, M. Deyo-Svendsen, Jet-induced cratering of a granular surface with application to lunar spaceports, J. Aerosp. Eng. 22 (2009) http://dx.doi.org/10.1061/(ASCE)0893-1321(2009)22:1(24).
- [52] P.T. Metzger, R.C. Latta, J.M. Schuler, C.D. Immer, M. Nakagawa, S. Luding, Craters formed in granular beds by impinging jets of gas, in: AIP Conference Proceedings, AIP, 2009, http://dx.doi.org/10.1063/1.3180041.
- [53] P.T. Metzger, J.E. Lane, C.D. Immer, Modification of roberts' theory for rocket exhaust plumes eroding lunar soil, in: Earth & Space 2008, 2008, pp. 1–8, http://dx.doi.org/10.1061/40988(323)4.
- [54] P.T. Metzger, J.E. Lane, C.D. Immer, J.N. Gamsky, W. Hauslein, X. Li, R.C. Latta III, C.M. Donaue, Scaling of erosion rate in subsonic jet experiments and apollo lunar module landings, in: Earth & Space 2010, 2010, pp. 191–207, http://dx.doi.org/10.1061/41096(366)21.
- [55] C. Immer, P. Metzger, Rocket cratering in simulated lunar and martian environments, in: Earth & Space 2010, 2010.
- [56] P.T. Metzger, R. Mueller, Landing plume effects, in: B.G. Drake (Ed.), Human Exploration of Mars Design Reference Architecture 5.0 Addendum, NASA Johnson Space Center, 2009.
- [57] J. Vessaire, G. Varas, S. Joubaud, R. Volk, M. Bourgoin, V. Vidal, Stability of a liquid jet impinging on confined saturated sand, Phys. Rev. Lett. 124 (2020) 224502, http://dx.doi.org/10.1103/PhysRevLett.124.224502.
- [58] C.Q. LaMarche, J.S. Curtis, Cratering of a particle bed by a subsonic turbulent jet: Effect of particle shape, size and density, Chem. Eng. Sci. (ISSN: 0009-2509) 138 (2015) 432–445, http://dx.doi.org/10.1016/j.ces.2015.08.030.
- [59] N. Rajaratnam, S. Beltaos, Erosion by impinging circular turbulent jets, J. Hydraul. Div. 103 (10) (1977) 1191–1205, http://dx.doi.org/10.1061/JYCEAJ. 0004852
- [60] P.T. Metzger, J. Smith, J.E. Lane, Phenomenology of soil erosion due to rocket exhaust on the moon and the mauna kea lunar test site, J. Geophys. Res. Planets 116 (E6) (2011) http://dx.doi.org/10.1029/2010JE003745.
- [61] J.E. Lane, P.T. Metzger, Estimation of apollo lunar dust transport using optical extinction measurements, Acta Geophys. 63 (2) (2015) 568–599, http://dx.doi. org/10.1515/acgeo-2015-0005.
- [62] P.T. Metzger, Erosion rate of lunar soil under a landing rocket, part 1: Identifying the rate-limiting physics, Icarus (ISSN: 0019-1035) 417 (2024) 116136, http://dx.doi.org/10.1016/j.icarus.2024.116136.
- [63] P.T. Metzger, Erosion rate of lunar soil under a landing rocket, part 2: Benchmarking and predictions, Icarus (ISSN: 0019-1035) 417 (2024) 116135, http://dx.doi.org/10.1016/j.icarus.2024.116135.
- [64] M. Mehta, N. Renno, A. Cotel, M. Grover, Characterization of the impingement dynamics of pulsed rocket plumes with the ground at low ambient pressure, in: 43rd AIAA/ASME/SAE/ASEE Joint Propulsion Conference &; Exhibit, 2007, http://dx.doi.org/10.2514/6.2007-5707.
- [65] D.H. Plemmons, M. Mehta, B.C. Clark, S.P. Kounaves, L.L. Peach Jr., N.O. Renno, L. Tamppari, S.M.M. Young, Effects of the phoenix lander descent thruster plume on the martian surface, J. Geophys. Res. Planets 113 (E3) (2008) http://dx.doi.org/10.1029/2007JE003059.
- [66] A. Sengupta, J. Kulleck, S. Sell, J.V. Norman, M. Mehta, M. Pokora, Mars lander engine plume impingement environment of the mars science laboratory, in: 2009 IEEE Aerospace Conference, 2009, pp. 1–10, http://dx.doi.org/10.1109/ AERO.2009.4839345.
- [67] M. Mehta, N.O. Renno, J. Marshall, M. Rob Grover, A. Sengupta, N.A. Rusche, J.F. Kok, R.E. Arvidson, W.J. Markiewicz, M.T. Lemmon, P.H. Smith, Explosive erosion during the phoenix landing exposes subsurface water on mars, Icarus (ISSN: 0019-1035) 211 (1) (2011) 172–194, http://dx.doi.org/10.1016/j.icarus. 2010.10.003.
- [68] J. Vizcaino, M. Mehta, Quantification of plume-soil interaction and excavation due to the mars science laboratory sky crane descent phase, in: 8th Symposium on Space Resource Utilization. 2015. http://dx.doi.org/10.2514/6.2015-1649.
- [69] P.T. Metzger, Rocket exhaust blowing soil in near vacuum conditions is faster than predicted by continuum scaling laws, in: Earth & Space 2016, 2016, pp. 58–66, http://dx.doi.org/10.1061/9780784479971.007.
- [70] S. Badr, G. Gauthier, P. Gondret, Crater jet morphology, Phys. Fluids (ISSN: 1070-6631) 28 (3) (2016) 033305. http://dx.doi.org/10.1063/1.4943160.
- [71] W.A. Chambers, P.T. Metzger, Regolith instability caused by gas diffusion: A case study of the asteroid redirect mission, in: Earth & Space 2016, 2016, pp. 67–73, http://dx.doi.org/10.1061/9780784479971.008.

- [72] S.D. Guleria, D.V. Patil, Experimental investigations of crater formation on granular bed subjected to an air-jet impingement, Phys. Fluids (ISSN: 1070-6631) 32 (5) (2020) http://dx.doi.org/10.1063/5.0006613, 053309.
- [73] M. Kuhns, P.T. Metzger, A. Dove, J. Byron, S. Lamb, T. Roberson, L. Lohman, W. Chambers, G. Rixon, R. Kuhns, M. Mehta, P. van Susante, Deep regolith cratering and plume effects modeling for lunar landing sites, in: Earth & Space 2021, 2021, pp. 62–78, http://dx.doi.org/10.1061/9780784483374.007.
- [74] P. Metzger, A. Dove, M. Conroy, J. Gloria, A. O'Reilly, A.S. John, Ejecta sheet tracking, opacity, and regolith maturity (ejecta storm): an instrument for lunar landing plume effects and dust dynamics, in: 52nd Lunar and Planetary Science Conference. 2021.
- [75] P.T. Metzger, J.G. Mantovani, The damage to lunar orbiting spacecraft caused by the ejecta of lunar landers, in: Earth & Space 2021, 2021, pp. 136–145, http://dx.doi.org/10.1061/9780784483374.014.
- [76] N. Rajaratnam, K. Mazurek, Impingement of circular turbulent jets on rough boundaries, J. Hydraul. Res. 43 (2005) http://dx.doi.org/10.1080/ 00221680509500388.
- [77] M. Baba, S. Okita, K. Watanabe, Y. Maru, S. Sawai, O. Mori, K. Fujita, Microgravity experiment using drop tower and CFD-dem coupled simulation about plume-surface interaction, in: AIAA SCITECH 2023 Forum, 2023, http://dx.doi.org/10.2514/6.2023-1785.
- [78] K.T. Edquist, S.J. Alter, C.E. Glass, B. Kleb, A.M. Korzun, W.A. Wood, F. Canabal, R.E. Childs, L.D. Halstrom, K.V. Matsuno, Computational modeling of mars retropropulsion concepts in the langley unitary plan wind tunnel, in: AIAA Science and Technology Forum and Exposition, AIAA SciTech Forum 2022, 2022, http://dx.doi.org/10.2514/6.2022-0912.
- [79] C.J. Eberhart, J. West, A.M. Korzun, Overview of plume-surface interaction data from subscale inert gas testing at NASA msfc test stand 300 vacuum facilities, in: AIAA SCITECH 2022 Forum, 2022, http://dx.doi.org/10.2514/6.2022-1811.
- [80] J.S. Rubio, M. Gorman, M.X. Diaz-Lopez, R. Ni, Plume-surface interaction physics focused ground test 1: Setup and preliminary results, in: AIAA SCITECH 2022 Forum, 2022, http://dx.doi.org/10.2514/6.2022-1809.
- [81] M.T. Gorman, J.S. Rubio, M.X. Diaz-Lopez, W.A. Chambers, A.M.K.M.J. Rabinovitch, R. Ni, Scaling laws of plume-induced granular cratering, PNAS Nexus (ISSN: 2752-6542) 2 (9) (2023) pgad300, http://dx.doi.org/10.1093/pnasnexus/pgad300.
- [82] N.S. Rodrigues, O.K. Tyrrell, P.M. Danehy, C. Eberhart, K.J. McDougal, T.Y. Liu, T.D. Reynolds, J.S. Rubio, N. Jiang, P. Hsu, A.M. Korzun, Flow visualization for plume-surface interaction testing within large-scale vacuum environments at conditions relevant to lunar and martian landers, in: JANNAF Exhaust Plume and Signatures Annual Meeting, 2023.
- [83] N.S. Rodrigues, O.K. Tyrrell, C. Eberhart, K.J. McDougal, A. Korzun, P.M. Danehy, Flow visualization for plume surface interaction at martian-relevant lander environments, in: AIAA Aviation FORUM and ASCEND 2024, 2024, http://dx.doi.org/10.2514/6.2024.4914
- [84] O.K. Tyrrell, N.S. Rodrigues, A.M. Korzun, P.M. Danehy, Flow visualization of intrusive and non-intrusive configurations for lunar- and martian-relevant plume-surface interaction, in: AIAA SCITECH 2024 Forum, 2024, http://dx.doi. org/10.2514/6.2024-2499.
- [85] D. Stubbs, L. Silwal, B.S. Thurow, M. Hirabayashi, V. Raghav, D. Scarborough, Non-intrusive, 3D optical measurements of crater formation due to plumesurface interactions, in: AIAA Scitech 2021 Forum, 2021, http://dx.doi.org/ 10.2514/6.2021-0831.
- [86] D.C. Stubbs, L. Silwal, B.S. Thurow, M. Hirabayashi, V. Raghav, D.E. Scar-borough, Three-dimensional measurement of the crater formation during plume–surface interactions using stereo-photogrammetry, AIAA J. 60 (3) (2022) 1316–1331, http://dx.doi.org/10.2514/1.J060835.
- [87] D. Stubbs, L. Silwal, V.N. Bhargav, B.S. Thurow, M. Hirabayashi, V. Raghav, D.E. Scarborough, Non-intrusive, 3-D crater formation measurements due to plume-surface interactions under sub-atmospheric pressure conditions, in: AIAA SCITECH 2023 Forum, 2023, http://dx.doi.org/10.2514/6.2023-2488.
- [88] L. Silwal, V.N. Bhargav, D.C. Stubbs, B.K. Fulone, B.S. Thurow, D.E. Scarborough, V. Raghav, Ejecta behavior during plume-surface interactions under rarefied atmospheric conditions, Acta Astronaut. (ISSN: 0094-5765) 218 (2024) 35–46, http://dx.doi.org/10.1016/j.actaastro.2024.02.013.
- [89] T. Crane, D. Stubbs, B.S. Thurow, V. Raghav, Three-dimensional crater formation measurements during plume-surface interaction in a reduced gravity environment using a drop tower, in: AIAA SCITECH 2024 Forum, 2024, http://dx.doi.org/10.2514/6.2024-2525.
- [90] N. Rasmont, H.T. Al-Rashdan, G. Elliott, J. Rovey, L.V. Roca, Millimeter wave interferometry for ejecta concentration measurements in plume-surface interactions, in: AIAA SCITECH 2022 Forum, 2022, http://dx.doi.org/10.2514/ 6.2022-2421.
- [91] N. Rasmont, H. Al-Rashdan, G.S. Elliott, J. Rovey, L.V. Roca, Spatially distributed measurements of ejecta concentrations in plume-surface interactions using millimeter wave interferometry, in: AIAA SCITECH 2023 Forum, 2023, http://dx.doi.org/10.2514/6.2023-0465.
- [92] N. Rasmont, H. Al-Rashdan, G. Elliott, J.L. Rovey, L.V. Roca, Millimeter-wave tomographic interferometry of ejecta concentrations in plume-surface interactions, in: AIAA SCITECH 2024 Forum, 2024, http://dx.doi.org/10.2514/6.2024-1979.

- [93] C. White, H. Zare-Behtash, K. Kontis, T. Ukai, J. Merrifield, D. Evans, I. Coxhill, T. Langener, J.V. den Eynde, Test facility to investigate plume-regolith interactions, in: International Conference on Flight Vehicles, Aerothermodynamics and Re-Entry Missions & Engineering, 2019.
- [94] C.J. Cuesta, D. Pickles, K. Worrall, A. Cammarano, H. Zare-Behtash, Characterisation of the dust cloud during landing on lunar and martian surfaces, in: Aerospace Europe Conference, 2023, http://dx.doi.org/10.13009/EUCASS2023-823.
- [95] C.J. Cuesta, J. Davies, K. Worrall, A. Cammarano, H. Zare-Behtash, Development of diagnostic techniques for plume-generated dust clouds, in: International Planetary Probe Workshop 2024, 2024, URL https: //www.openconf.org/ippw2024/modules/request.php?module=oc_program& action=summary.php&id=37.
- [96] R. Greeley, R. Leach, B. White, J. Iversen, J. Pollack, Threshold windspeeds for sand on mars: Wind tunnel simulations, Geophys. Res. Lett. 7 (2) (1980) 121–124, http://dx.doi.org/10.1029/GL007i002p00121.
- [97] T. Ukai, S. Subramanian, A. Wilson, B. Craig, K. Kontis, Initial particle ejection behaviours due to a hypersonic jet impingement at different highnozzle pressure ratios in rarefied atmospheric conditions, Acta Astronaut. (ISSN: 0094-5765) 222 (2024) 126–135, http://dx.doi.org/10.1016/j.actaastro.2024. 06.009.
- [98] M. Mehta, A. Sengupta, M. Pokora, L. Hall, N. Renno, Mars landing engine plume impingement ground interaction, in: Earth & Space 2010, 2010, pp. 143–157, http://dx.doi.org/10.1061/41096(366)17.
- [99] A.M. Korzun, C.J. Eberhart, J. West, P. Liever, A. Weaver, J. Mantovani, A. Langton, B. Kemmerer, A. Atkins, Design of a subscale, inert gas test for plume-surface interactions in a reduced pressure environment, in: AIAA SCITECH 2022 Forum, 2022, http://dx.doi.org/10.2514/6.2022-1808.
- [100] M.X. Diaz-Lopez, M. Gorman, J.S. Rubio, R. Ni, Plume-surface interaction physics focused ground test 1: Diagnostics and preliminary results, in: AIAA SCITECH 2022 Forum, 2022, http://dx.doi.org/10.2514/6.2022-1810.
- [101] S. Subramanian, A. Wilson, C. White, K. Kontis, D. Evans, J. Van den Eynde, Tracking plume-regolith interactions in near-vacuum conditions, Phys. Fluids (ISSN: 1070-6631) 36 (1) (2024) 013301, http://dx.doi.org/10.1063/5. 0180669
- [102] H. Al-Rashdan, Supersonic underexpanded flow visualization in sub-atmospheric facility, in: AIAA Aviation 2021 Forum, 2021, http://dx.doi.org/10.2514/6. 2021-2859
- [103] P.T. Metzger, X. Li, C. Immer, J. Lane, ISRU implications for lunar and martian plume effects, in: 47th AIAA Aerospace Sciences Meeting Including the New Horizons Forum and Aerospace Exposition, American Institute of Aeronautics and Astronautics, 2009, http://dx.doi.org/10.2514/6.2009-1204.
- [104] P.A. Longwell, Mechanics of Fluid Flow, McGraw-Hill, 1966.
- [105] A. Martin, C. Wagoner, Lunar simulant assessment, in: Johns Hopkins Applied Physics Laboratory Lunar Surface Innovation Consortium, 2022.
- [106] M. Raffel, Background-oriented schlieren (BOS) techniques, Exp. Fluids (2015) http://dx.doi.org/10.1007/s00348-015-1927-5.
- [107] R. Haehnel, W.B. Dade, Particle entrainment by non-uniform eolian flow, in: Earth and Space 2010, 2010, pp. 158–165, http://dx.doi.org/10.1061/ 41006(266)18
- [108] NASA, Classifications and requirements for testing systems and hardware to be exposed to dust in planetary environments, in: NASA-STF-1008, 2021.

- [109] J. You, X. Zhang, H. Zhang, C. Li, Y. Xu, Q. Yan, H. Yu, J. Liu, Y. Li, Y. Wang, C. Zhao, H. Zhang, Y. Xu, L. Chen, H. Lin, Q. Fu, Y. Gao, Y. Wang, W. Wang, Q. Zhi, Analysis of plume-lunar surface interaction and soil erosion during the Chang'E-4 landing process, Acta Astronaut. (ISSN: 0094-5765) 185 (2021) 337-351. http://dx.doi.org/10.1016/j.actaastro.2021.05.009.
- [110] E.-R.A. University, EagleCam, 2024, URL https://erau.edu/eaglecam.
- [111] NASA, Stereo cameras for lunar plume surface studies, 2022, URL https://nssdc.gsfc.nasa.gov/nmc/experiment/display.action?id=IM-1-NOVA-01.
- [112] R.J. Thompson, P.M. Danehy, M.M. Munk, M. Mehta, M.S. Manginelli, C. Nguyen, O.H. Thomas, Stereo camera simulation for lunar surface photogrammetry, in: AIAA SCITECH 2021 Forum, 2021.
- [113] O.K. Tyrrell, R.J. Thompson, P.M. Danehy, C.J. Dupuis, M.M. Munk, C.P. Nguyen, R.W. Maddock, T.W. Fahringer, W.C. Krolick, A. Weaver, J. West, M.S. Manginelli, W.K. Witherow, Design of a lunar plume-surface interaction measurement system, in: AIAA SCITECH 2022 Forum, 2022, http://dx.doi.org/10.2514/6.2022-1693.
- [114] O.K. Tyrrell, J. Weisberger, T. Fahringer, P. Danehy, R. Maddock, C. Nguyen, M. Munk, M. Manginelli, W. Witherow, Stereo cameras for lunar plume-surface studies: First lunar flight mission, in: International Planetary Probe Workshop 2024, 2024, URL https://www.openconf.org/ippw2024/modules/request.php? module=oc_program&action=summary.php&id=42.
- [115] J. Kim, M. Jeong, M. Kim, Y. Kim, Y. Choi, S.S. Kim, D. Lee, B. Moon, D. Lee, S. Choi, C.K. Sim, S. Baek, M. Lee, Current status of SurfCam development, in: Photonic Instrumentation Engineering XI, Vol. 12893, SPIE, 2024, 1289302.
- [116] R.E. Peale, C.J. Fredricksen, C.L. Barrett, A.G. Otero, A.R. Jack, F.J. Gonzalez, D. Sapkota, A.R. Dove, P.T. Metzger, Laser particle sizer for plume-induced ejecta clouds, in: G.W. Kamerman, L.A. Magruder, M.D. Turner (Eds.), Laser Radar Technology and Applications XXVII, Vol. 12110, SPIE, International Society for Optics and Photonics, 2022, http://dx.doi.org/10.1117/12.2618322.
- [117] R.E. Peale, D. Hathnagoda, C. Kelley, C.J. Fredricksen, C. Walker, C. Posada, J. Zorovich, C. Cariker, N. Dhakal, J. Gonzalez, P. Golvari, S.M. Kuebler, P. Metzger, A. Dove, Laser particle sizer for lunar plume-surface interaction studies, in: G.W. Kamerman, L.A. Magruder, M.D. Turner (Eds.), Laser Radar Technology and Applications XXVIII, Vol. 12537, SPIE, International Society for Optics and Photonics, 2023, http://dx.doi.org/10.1117/12.2663930.
- [118] A.G. Langton, J.G. Mantovani, B.W. Kemmerer, A.R. Atkins, D.P. Batcheldor, A millimeter wave Doppler radar to measure plume surface interactions ejecta velocities, in: ASCEND 2022, 2022, http://dx.doi.org/10.2514/6.2022-4282.
- [119] B.W. Kemmerer, A.G. Langton, J.G. Mantovani, A.R. Atkins, D.P. Batcheldor, G.L. Bastin, Development of the dust ejecta radar technology (DERT) to determine plume-surface interaction ejecta velocities on planetary surfaces, in: 2023 IEEE International Radar Conference, 2023.
- [120] A. Bueno, M.J. Krasowski, N. Prokop, L.C. Greer, C.M. Adams, N.O. Rennó, Instrument to study plume surface interactions (PSI) on the lunar surface: Science motivation, requirements, instrument overview, and test plans, Aerospace 11 (6) (2024) http://dx.doi.org/10.3390/aerospace11060439.
- [121] NASA, Humans to mars, 2024, URL https://www.nasa.gov/humans-in-space/humans-to-mars/#:~:text=NASA%20is%20advancing%20many% 20technologies, to%20the%20Red%20Planet%20possible.